Journal of the Australian Ceramic Society
https://doi.org/10.1007/s41779-019-00345-3

RESEARCH

The effect of alumina additive and sintering temperature on the microstructural, physical, mechanical, and bioactivity properties of hydroxyapatite–alumina composites

Suleyman Serdar Pazarlioglu[1] · Serdar Salman[1,2]

Received: 13 September 2017 / Revised: 14 February 2019 / Accepted: 13 March 2019
© Australian Ceramic Society 2019

Abstract
The aim of this study was to evaluate the effect of alumina (Al_2O_3) additive and sintering temperature on the microstructural, physical, mechanical, and in vitro bioactivity properties of hydroxyapatite (HA). The composites consisting of 2.5 and 5 wt% Al_2O_3 and monolithic HA were uniaxially pelleted at 350 MPa with the size of ∅11 and 11 mm^2 and sintered at five different temperatures ranging from 900 to 1300 °C for 4 h. A series of thermal analysis methods and tests were used to evaluate both phase changes that occurred during sintering and the physical/mechanical properties of the sintered samples. The bioactivity property of the samples having the highest compressive strength value was investigated in a simulated body fluid (SBF) solution for 3, 7, 15, and 30 days. Results showed that HA without Al_2O_3 had started to decompose at 1200 °C, and the addition of Al_2O_3 led to the reduction of decomposition temperature from 1200 to 900 °C. However, the main phase was HA for all the sintered samples. The highest mechanical strength values were 130.20 ± 6.22, 60.27 ± 9.93, and 0.96 ± 0.05 MPa $m^{1/2}$ for compressive strength, three-point bending strength, and fracture toughness, respectively, for monolithic HA when it was sintered at 1100 °C. All of these mechanical strength values of monolithic HA were improved higher than the rate of 60% as the grain growth of HA was inhibited by the addition of Al_2O_3. The highest mechanical strength values of HA–Al_2O_3 composites were obtained for the samples sintered at 1200 °C when the densification rate reached 90%. In vitro investigations showed that Al_2O_3 led to a reduction in the in vitro bioactivity of HA, but it could be used in the human body since its surface is coated by apatite layers when in vitro time reached 30 days.

Keywords Hydroxyapatite · Alumina · Sintering

Introduction

Humans begin to age from the moment they are born and they can face serious problems that can affect their quality of life due to the reasons of traffic, occupational, and/or sportive accidents [1]. The repair of bone defects is a common clinical problem and more than 500,000 of bone repair are performed annually worldwide as reported by Kamitakahara et al. [2]. Current lines of treatment such as autogenous bone grafts, which involve the transplantation of bone from another part of the patient, or allografts, where bone tissue is taken from donors or cadavers, are affected by specific drawbacks, i.e., donor site morbidity, disease transmission risks, high costs, and potential complications like infections [3]. It was reported in the 1970s that hydroxyapatite (HA) has excellent biocompatibility due to its similarity to the inorganic tissue of the matrix of bone and its chemical and crystallographic structure. Moreover, HA can integrate into bone structures, supporting bone in-growth without breaking down or dissolving, and it interacts with the living tissue due to the presence of free calcium and phosphate compounds. This property makes HA extremely attractive and widely used as a material for bone implants [4]. HA has different mechanical properties in different ranges depending on the sintering temperature and duration used. Compressive strength between 133 and

✉ Suleyman Serdar Pazarlioglu
spazarlioglu@marmara.edu.tr

[1] Technology Faculty, Metallurgy and Materials Engineering, Marmara University, Goztepe Campus, 34722 Istanbul, Turkey

[2] National Defense University, 34334 Beşiktaş, Istanbul, Turkey

Published online: 08 April 2019

193 MPa, bending strength between 38 and 250 MPa, and tensile strength between 49 and 174 MPa have been reported for HA in the literature. These results were also affected by porosity, impurity, and test directions according to the bone axis, etc. Modulus of elasticity had a range from 11.5 to 27 GPa showing that HA is a brittle material. The fracture toughness for HA was reported between 0.6 and 1 MPa $m^{1/2}$, whereas these values are between 2 and 12 MPa $m^{1/2}$ for bone [5]. Despite of the biological advantages of HA, solid HA cannot be used to repair defects in load-bearing bones mainly due to its low fracture toughness (less than 1 MPa $m^{1/2}$) when compared to cortical bone [6]. Clinical applications of HA might be expanded by exploiting or improving appropriate mechanical properties [7]. It is well known that the incorporation of a ceramic reinforcement (i.e., fibers, whiskers, platelets, or particles) in a ceramic matrix improves the mechanical properties [8]. To be effective as a reinforcing agent for a ceramic–matrix material, the following conditions should be satisfied:

- The strength of the second phase must be higher than that of the matrix. Second, the interfacial strength between the matrix and the second phase should be neither too weak nor too strong.
- For an appropriate interfacial strength, no excessive reaction should occur between the matrix and the second phase.
- The coefficient of thermal expansion (CTE) of the second phase should not differ too much from that of the matrix.
- In the case of biomaterials, the biocompatibility of the reinforcing agent is another important factor that should be considered [9].

Alumina (Al_2O_3) is one of the most widely used structural ceramic materials in the various fields of the industry due to its good mechanical properties, excellent oxidation resistance, and corrosion resistance [10]. Al_2O_3 has been also successfully used for 30 years in orthopedics and dentistry as a bioceramic due to its high wear resistance, bioinertness, and chemical durability, but it does not bond to living tissue when implanted [11–13]. Moreover, Al_2O_3 has better mechanical properties than HA [14–16] as shown in Table 1. The composites of Al_2O_3-doped HA-based bioceramics do not have any negative effect on cell proliferation as stated in previous studies [17–19].

Table 1 Physical and mechanical properties of Al_2O_3 and HA

Property	Al_2O_3 [14, 15]	HA [5, 16]
Density (g/cm^3)	3.90–3.93	2.55–3.156
Hardness (GPa)	18–20	4.2–4.5
Bending strength (MPa)	400–550	38–250
Young's modulus (GPa)	310–410	11.5–22
Fracture toughness (MPa $m^{-1/2}$)	5–6	0.6–1
Compressive strength (MPa)	690–5500	133–193

The purpose of the present study was to investigate the microstructural, mechanical, and in vitro bioactivity properties of hydroxyapatite with and/or without alumina additives that were in different weight compositions. Mechanisms of reactions between hydroxyapatite and alumina were deduced from X-ray diffraction, scanning electron microscopy, and a series of mechanical tests such as density, hardness, compressive strength, three-point bending strength, and fracture toughness measurements. In vitro bioactivity tests were also performed for the samples, which have the mechanical properties that can be used in the human body, in a simulated body fluid solution for 3, 7, 15, and 30 days.

Experimental procedure

Sample preparation

The starting powders were HA (Acros Organics, CAS number: 1306-06-5) and Al_2O_3 (Sigma Aldrich, CAS Number: 1344-28-1, 99.5% purity) in the present study. According to the information given by Acros Organics, HA powder consists of As (≤ 2 ppm), Hg (≤ 1 ppm), Pb (≤ 5 ppm), Cd (≤ 2 ppm), Cl (≤ 1500 ppm), Cu (≤ 20 ppm), F (≤ 50 ppm), Fe (≤ 400 ppm), SO_4^{2-} (≤ 5000 ppm), Ca (39.894 wt%), and P (18.498). It can be used for biomedical applications as the rates of impurities are compatible with ASTM F1185-88 standards [20], and it is in good agreement with stoichiometric HA because its Ca/P molar ratio is 1.667 [21]. Figure 1 shows the SEM images of HA and Al_2O_3 powders. HA has numerous agglomerated particulates of irregular form and an average grain size of 7.096 ± 1.15 μm, and Al_2O_3 has an alpha structure of irregular form and an average grain size of 8.334 ± 0.393 μm, as shown in Fig. 2; it indicates similar median particle sizes for the two types of powder.

Figure 3 shows the XRD analysis of HA and Al_2O_3 powders, respectively. As shown in Fig. 3a, HA does not include secondary phases such as beta- or alpha-tricalcium phosphate (β- or α-TCP) or tetracalcium phosphate (TTCP) and calcium oxide (CaO) at room temperature. The XRD analysis of the Al_2O_3 powder used as the reinforcement material for HA shows that the peaks at 2θ of 35.1, 37.7, 43.3, 52.5, 57.4, 66.4, 68.1, and 76.8 are related to α-alumina and are compatible with JCPDS 98-004-0109. In the light of literature reviews, the amount of Al_2O_3 selected was 2.5 and 5 wt% for the following reasons:

1. The addition of Al_2O_3 to HA at a high ratio (more than 5 wt%) causes the formation of secondary phases and crack formations at a high rate.

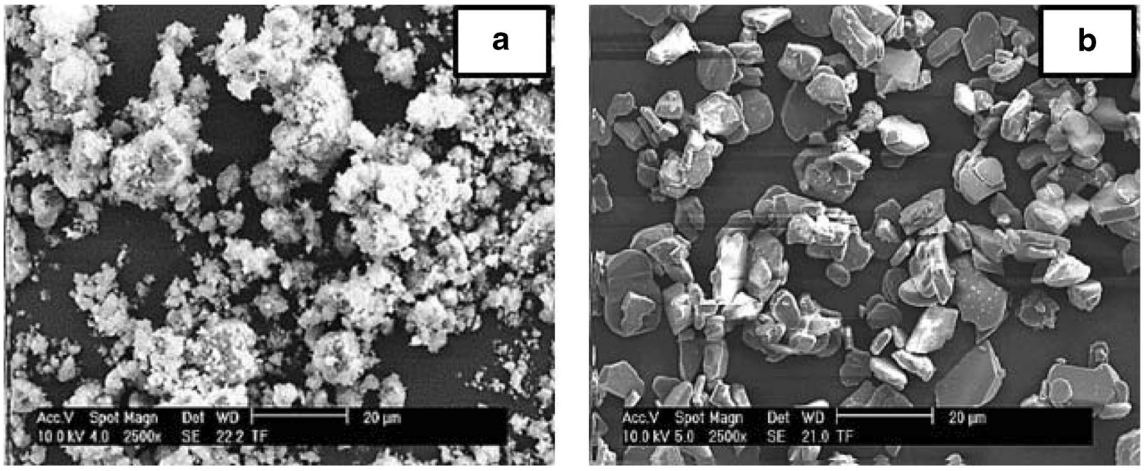

Fig. 1 SEM images of **a** HA and **b** Al_2O_3 powders

2. The addition of Al_2O_3 at an amount more than 5 wt% to HA also leads to increase the time for the formation of apatite layers on the surface of HA. For this reason, the bioactivity of HA influences negatively [22, 23].

The powders were mixed using a conventional ball milling at 180 rpm for 2 h to obtain the HA–Al_2O_3 composites. Mixture powders were firstly dried at 105 °C for 24 h and then pelleted at 350 MPa (under the load of ≈ 3.32 tons) to obtain green bodies according to British Standards (BS 7253) [24]. The dimensions of the green bodies are 11 mm in diameter and 11 mm in height. Finally, the green bodies were sintered in air condition at sintering temperatures of 900, 1000, 1100, 1200, and 1300 °C, at a ramp rate of 5 °C and soaking time of 4 h, and then cooled to room temperature at a ramp rate of 5 °C at air atmosphere.

Determination of the microstructural changes

Phase analysis was performed to the powders obtained from compression test samples crushed by using agate mortar. XRD analyses were conducted by a Philips X'Pert X-ray diffraction machine at room temperature using Cu-Kα as the radiation source at a scan speed of 0.6° per minute and a step scan of 0.02° in the range of 2θ values between 25° and 50°. The percentage of the phases detected by XRD analysis was determined by Rietveld analysis. The changes in the surface morphology of the sintered samples were determined by FEI Sirion XL30 SEM machine. The changes in the average grain size of the sintered samples were determined by the linear intercept method [25], and the activation energy for grain growth on the surface-sintered samples was calculated using Eq. 2.1.

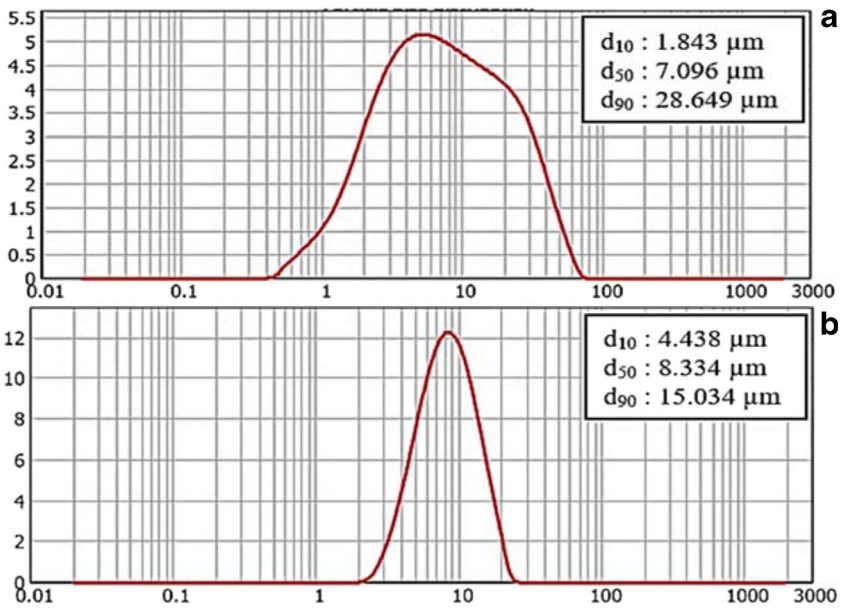

Fig. 2 Particle size of **a** HA and **b** Al_2O_3 powder

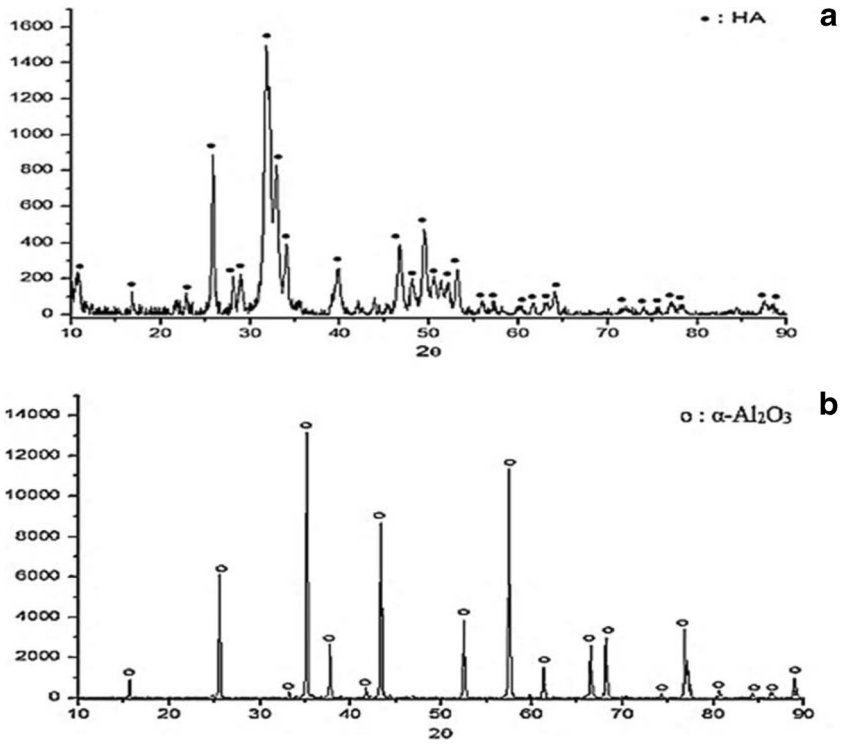

Fig. 3 XRD analysis of **a** monolithic HA and **b** Al_2O_3 powder at room temperature

$$D = D_o \exp[-Q/RT] \tag{2.1}$$

Where D is the average grain size (μm), D_o is the material constant, Q is the activation energy required for grain growth (kJ/mol), R is the gas constant (8.314 kJ/mol), and T is the temperature (K) [26].

Determination of the physical and mechanical properties

In order to determine the physical and mechanical properties of the sintered samples, the measurements of green, apparent and relative density, porosity, shrinkage, hardness, fracture toughness, three-point bending, and compressive strength were performed. While the green densities were calculated by the dividing of mass to volume using Eq. 2.2, apparent density and % porosity ratios of the sintered samples were calculated by the Archimedes method using Eqs. 2.3 and 2.4. Theoretical density values of the sintered samples were calculated using Eq. 2.5.

$$\text{Green density} = \frac{m}{\pi r^2 h} \tag{2.2}$$

where d is the green density (g/cm^3), m is the weight (g), r is the radius (mm), and h is the height (mm) of the pelleted samples.

$$\text{Apparent density} = \frac{\text{Mk}}{\text{Ma}-\text{Ms}} \tag{2.3}$$

$$\%\text{porosity} = \left(\frac{\text{Ma}-\text{Mk}}{\text{Ma}-\text{Ms}}\right) \times 100 \tag{2.4}$$

where Mk is the dry weight (g), Ma is the wet weight of the sample, and Ms is the wet weight of the suspension in distilled water.

$$\text{Theoretical density} = \frac{m_t}{\left(\frac{m_1}{d_1} + \frac{m_2}{d_2}\right)} \tag{2.5}$$

where m_t is the total weight of the mixture (g), m_1 is the weight of HA in the mixture (g), d_1 is the theoretical density of HA (3.156 g/cm^3 [27]), d_2 is the theoretical density of Al_2O_3 (3.970 g/cm^3 [28]), and m_2 is the weight of Al_2O_3 in the mixture (g).

Calculation of % shrinkage ratios was carried out by comparison of the size of each sample before and after the sintering process with an electronic caliper which has 1/1000 sensitivity as shown in Eq. 2.6

$$\text{Shrinkage} = \left(\frac{L1-L2}{L1}\right) \times 100 \tag{2.6}$$

Where L_1 is the length before sintering (mm) and L_2 is the length after sintering (mm).

For hardness and fracture toughness measurements, the samples were firstly ground with 800, 1200, and 2500 mesh SiC paper and then polished with 10, 5, 3, and 1 μm diamond paste until mirror-like surfaces are obtained. They were calculated by a Shimadzu HMV2 device using loads of 200 and

300 g for 20 and 10 s according to Eqs. 2.7 and 2.8, respectively. Average and standard deviation values were taken from 20 indents.

$$\mathrm{HV} = 0.0018544\left(P/d^2\right) \tag{2.7}$$

Here, HV is the hardness (GPa), P is the applied force (N), and d is the average indentation diameter (mm^2),

$$K_{\mathrm{IC}} = 0.203(c/a)^{-1.5}(\mathrm{HV})(a)^{0.5} \tag{2.8}$$

Here, K_{IC} is the fracture toughness (MPa $m^{1/2}$), c is the radial crack dimension measured from the center of the indent impression (m), HV is the hardness (MPa), and a is the half diagonal of the indentation. K_{IC} values were calculated using the Niihara equation [29]. Compression tests were carried out to ten samples using a universal testing machine (Devotrans FU 50 kN, Turkey) under a loading rate of 2 mm/min. The three-point bending strength of the samples was determined using Eq. 2.9 at a crosshead speed of 1 mm/min until they were broken to specimens with the dimensions 40 × 4 × 4 mm^3 prepared according to ASTM C1161-94 standards at 160 MPa [30]. The inner ring had a diameter of 10 mm and the outer support ring had a diameter of 20 mm. The distance between inner spans was 20 mm. The sintered test bars were ground (1200 grit) on both sides before testing. Five specimens were tested for a single point.

$$\sigma_{\text{three-point bending}} = 3PL/2bh^2 \tag{2.9}$$

Here, P is the breaking load (N), L is the distance between inner spans (mm), b is the specimen width (mm), and h is the specimen thickness (mm).

In vitro bioactivity test

In this study, the in vitro bioactivity properties of the samples which have the highest compressive strength were determined by simulated body fluid (SBF) prepared according to Kokubo et al. [31]. Before the in vitro test, totally, four samples were sintered to the temperatures in which they attained the highest compressive strength value with the size of ∅11 and 4 mm^2. After this stage, the samples were ground by 400, 600, 800, 1000, and 1200 mesh SiC paper and then they were dried in an oven at 105 °C for 1 day. The samples were immersed in sealed test tubes containing 20 mL of SBF for 3, 7, 15, and 30 days. The 20-mL SBF solutions used in the in vitro tests were refreshed every day until the specified times were completed. When the specified times were completed, the samples were taken from SBF solutions without damaging the apatite layers and then cleaned by distilled water and finally dried at 60 °C for 12 h. Apatite layers occurring on the surface of the samples immersed in SBF solutions were investigated by SEM.

Results and discussion

Microstructural characterization

Figure 4 and Table 2 show the results of XRD and Rietveld analysis after sintering of monolithic HA at specific temperatures.

HA powder used as matrix material in the present study contained only HA peaks at sintering temperatures between 900 and 1100 °C. In addition to HA, β-TCP (compatible with the JCPDS card number of 98-007-6896) was detected for the sample sintered at 1200 °C. Moreover, α-TCP (compatible with the JCPDS card number of 98-007-8499) and CaO (compatible with the JCPDS card number of 98-003-4977) phases were detected at sintering temperature of 1300 °C, in addition to HA and β-TCP phases. The presence of β- or α-TCP and CaO phases reveals that HA starts to decompose at above 1100 °C. As indicated by Bemache-Assollant et al. [32], the formation of these second and/or third phases occurs as shown in Eq. 3.1

$$\mathrm{Ca_{10}(PO_4)_6(OH)_2 \rightarrow 3Ca_3(PO_4)_2 + CaO + H_2O} \tag{3.1}$$

HA decomposes to TCP and CaO phases [33]. The coexistence of HA+TCP and/or HA+CaO is due to the descending and/or exceeding of Ca/P molar ratio (1.667) of stoichiometric HA [34, 35]. Table 2 reveals that the amount of secondary phases that occurred in monolithic HA is less than 5%, and the main phase is HA in all sintering temperatures.

As shown in Table 3 and Fig. 5, the formation of dissimilar calcium aluminate phases at different 2θ angles due to the solid-state reactions between HA and Al_2O_3 powders was detected.

The term "calcium aluminate" is a nomenclature used for a series of compounds with different Ca/Al ratios [36]. Calcium aluminates have a wide range of application in the steel industry as metallurgical slags, in the cement industry as hydraulic materials, and in the refractory industry as ceramic materials [37] and as advanced ceramics such as optical ceramics, catalyst support, flame detectors, dental cement, and structural ceramics [38]. Apart from these applications, because of their good physical and mechanical properties and biocompatibility and because they act as a chemical and mechanical barrier against bacterial microleakage, they have been successfully used as an endodontic repairing biomaterial [39]. As a calcium aluminate compound, $Ca_3Al_2O_6$, which has a P_{m3m}-type body-centered cubic structure with the lattice parameter of $a = 7.626$ Å, occurs at low temperature (900–1100 °C) as a result of the solid-state reaction between CaO and Al_2O_3, and it has been used in applications where high-temperature resistance is required [40–42]. As stated by Liu and Chang, it contributes to the improvement of bioactivity and biocompatibility of dicalcium silicate (Ca_2SiO_4) when added to below

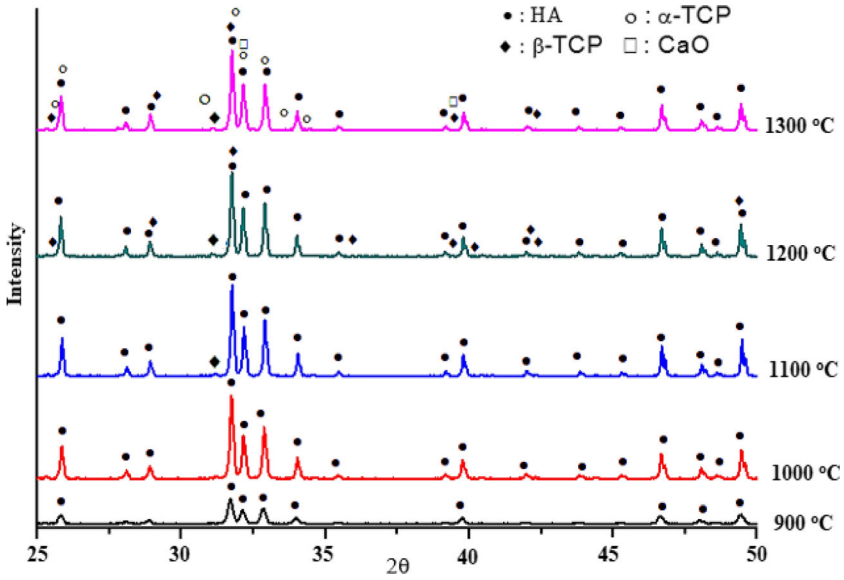

Fig. 4 XRD analysis results of the monolithic HA depending on the sintering temperatures

10% in weight [43]. $CaAl_4O_7$ is found in terrestrial rocks and meteorites and is named minerologically as grossite with a monoclinic structure of the type C2/c of $a = 1.289$ nm, $b = 0.889$ nm, $c = 0.544$ nm, and $\beta = 106.938$ [44, 45]. As pointed out by Gawalt et al., the oxide surface of $CaAl_4O_7$ has reactive groups, hydroxyl, and μ-oxo, available for easy attachment of organic acids which are the first step in the covalent linkage system for antibiotics [46], but their surface properties need to be improved in order to become bioactive [47]. $Ca_2Al_2O_5$ is a calcium aluminate compound which has an orthorhombic space group symmetry/2*mb*, $a = 5.626$ Å, $b = 14.698$ Å, $c = 5.419$ Å, and it belongs to the brownmillerite structure family that is used in applications as solid fuel batteries and in partial oxidation of hydrocarbons and in decomposition of oxygen from gas streams [48–50]. In HA–Al_2O_3 binary composites, $Ca_2Al_2O_5$ occurs according to Eq. 3.2 and it does not have any negative effect on the bioactivity property of the HA–Al_2O_3 system [51].

$$2CaO + Al_2O_3 \rightarrow Ca_2Al_2O_5 \tag{3.2}$$

$Ca_5Al_6O_{14}$ is a material with a catalyst effect in Ni/CaAlX compounds [52], and it occurs by solid-state reaction between CaO and Al_2O_3 [53]. $CaAl_2O_4$ is a refractory material occurring in CaO–Al_2O_3 binary system which has a monoclinic crystal system with space group $P2_1/n$ with lattice parameters of $a = 8.7$ Å, $b = 8.092$ Å, and $c = 15.191$ Å and it melts at 1602 °C [54–56]. $CaAl_2O_4$ has received considerable attention as a material for (implants) bone graft material, artificial tooth, and spine pieces due to its unique combination of physical and mechanical, bioactive, and biocompatible properties. Apart from these applications, it has also been used for the manufacturing of eyeglass components, but it has a negative effect on enhancing the decomposition of HA in HA–Al_2O_3 binary composites as seen in Eq. 3.3 [57–59].

$$Ca_{10}(PO_4)_6(OH)_2 + Al_2O_3 \rightarrow 3Ca_3(PO_4)_2 + CaAl_2O_4 + H_2O \tag{3.3}$$

As stated in previous studies, $CaAl_2O_4$ has enough mechanical resistance and negatively charged surface, and when it immerses in SBF solution, it contributes to the formations of katoite ($Ca_3Al_2(O_4H_3)$) and gibbsite ($(Al(OH)_3)$). These formations facilitate the deposition of apatite layer on the surface of implants in a short period of 1 day. Because of this property, it is also a bioactive phase [60, 61]. Solid-state reactions in ionic materials take place by the diffusion of ions across the interface. In the present case, Ca^{2+} and Al^{3+} are the important species for the formation of aluminates. There are two ways in which the reaction can take place. Al^{3+} can diffuse into the HA or Ca^{2+} can diffuse from the HA into the alumina [62]. The formation of the abovementioned calcium aluminate phases in the HA–Al_2O_3 binary compositions can be schematically illustrated as shown in Fig. 6.

As stated in Fig. 4, β-TCP was detected at 1200 °C for monolithic HA. However; it was found that β-TCP began to form from the sintering temperature of 900 °C for Al_2O_3-

Table 2 Detected phases and their amounts occurred in monolithic HA depending on sintering temperatures

	Phases and their amounts (%)	Sintering temperature (°C)				
		900	1000	1100	1200	1300
HA	HA	100	100	100	96.2	94.2
	β-TCP	–	–	–	3.8	4.1
	α-TCP	–	–	–	–	1.6
	CaO	–	–	–	–	0.1

Table 3 Detailed information on calcium aluminate phases formed

Type of calcium aluminate phase	The highest 2θ angles that are detected	XRD card number
$Ca_3Al_2O_6$	33.21°, 47.67°, and 59.33°	98-008-9635
$CaAl_4O_7$	25.46°, 19.98°, and 34.55°	98-001-4312
$Ca_2Al_2O_5$	34.39°, 48.43°, and 34.27°	98-005-6621
$Ca_5Al_6O_{14}$	30.57°, 31.02°, and 36.36°	98-000-0919
$CaAl_2O_4$	30.07°, 30.14°, and 35.42°	98-000-0144

added samples and its amount is increased by increasing sintering temperature and Al_2O_3 ratio. This means that Al_2O_3 addition leads to a reduction of the decomposition temperature of HA. As stated by Evis et al. [63], mixtures of HA and Al_2O_3 powders in micron size were sintered in air at temperatures ranging from 1100 to 1400 °C, and Al_2O_3 catalyzes the decomposition of HA with the formation of calcium aluminate. The solid solubility in Al_2O_3 is limited because of its closely packed structure; therefore, the formation of aluminates probably takes place on the surface of the alumina particles. The removal of calcium must be compensated by the formation of oxygen vacancies, which leads to HA

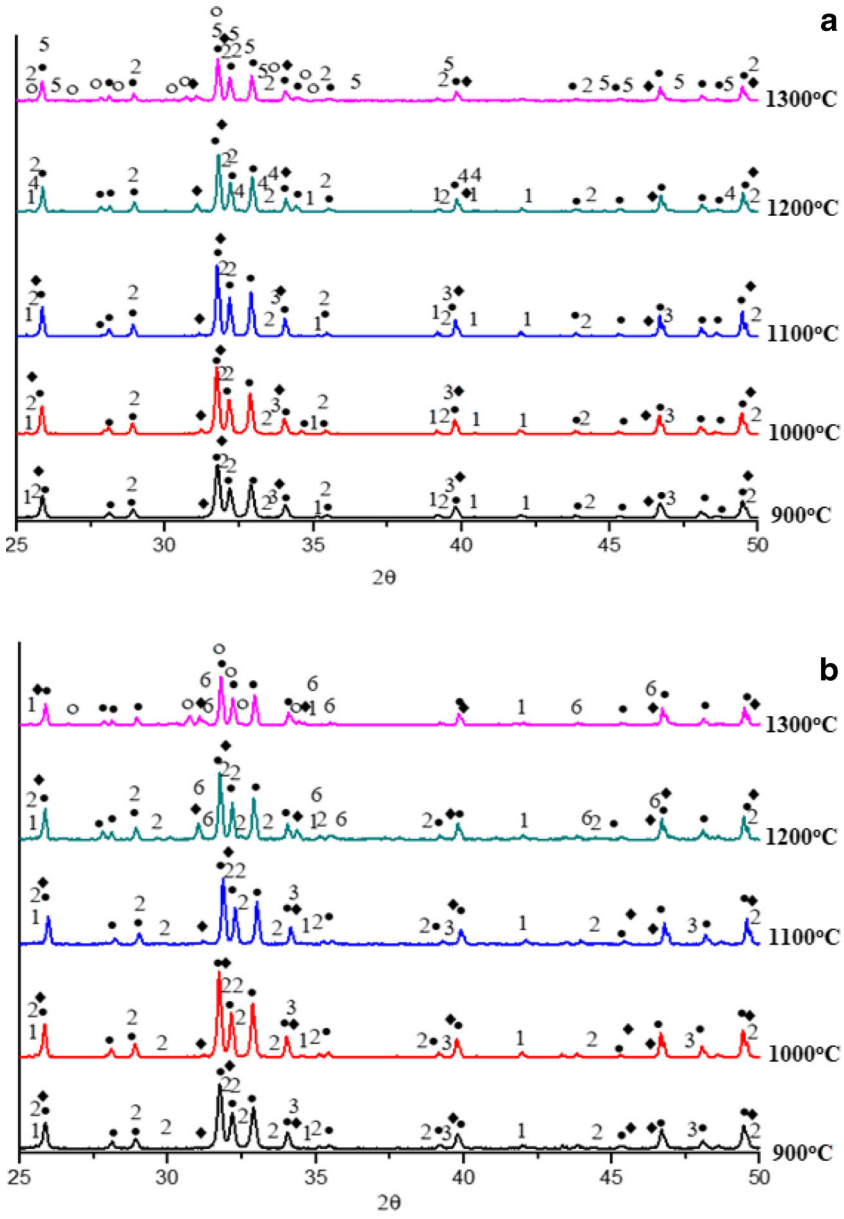

Fig. 5 XRD analysis of **a** HA–2.5A and **b** HA–5A binary composites (filled circle: HA, filled diamond: β-TCP, open circle: α-TCP, 1: α-Al_2O_3, 2: $CaAl_4O_7$, 3: $Ca_3Al_2O_6$, 4: $Ca_2Al_2O_5$, 5: $Ca_5Al_6O_{14}$, 6: $CaAl_2O_4$)

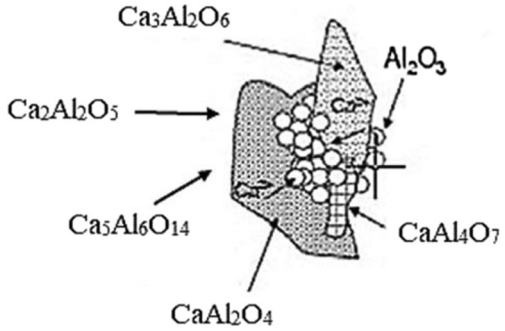

Fig. 6 Schematic representation of the formation of calcium aluminate phases in HA–Al_2O_3 binary composites

structure, and monolithic HA is converted to calcium-deficient HA (Ca/P = 1.5) as shown in Fig. 7.

The α-TCP phase was found at an only sintering temperature of 1300 °C for all samples. Moreover, it was determined that CaO formed as a result of the sintering of the monolithic HA at 1300 °C which did not occur at other sintering temperatures for Al_2O_3-added samples. In addition to the absence of the CaO phase at lower temperatures than 1300 °C, the reason for the lower rates of β-TCP and α-TCP phases (the amount of β-TCP and α-TCP in sintered samples) found in this study is due to the use of Al_2O_3 at a lower ratio than other HA–Al_2O_3 composites in the literature [64–66]. It was found by Rietveld analysis that the amount of HA in HA–Al_2O_3 binary composites decreased by increasing sintering temperatures and Al_2O_3 ratios as can be seen in Fig. 8a. The HA ratio in HA–2.5A decreased from 95.4 to 77.3%, while it decreased

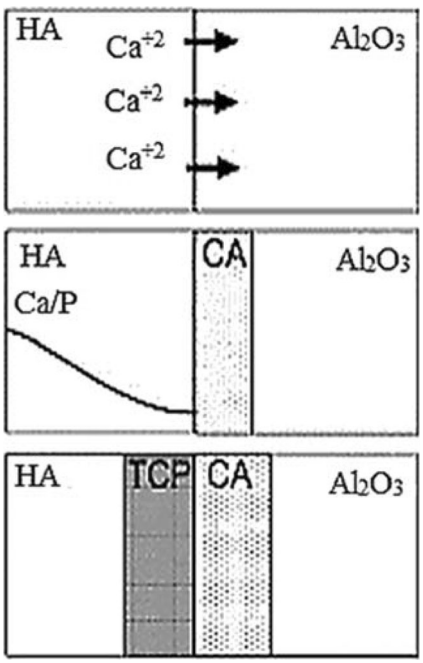

Fig. 7 Schematic representation of the formation of TCP and calcium aluminate phases due to the solid-state reaction between HA and Al_2O_3 powders

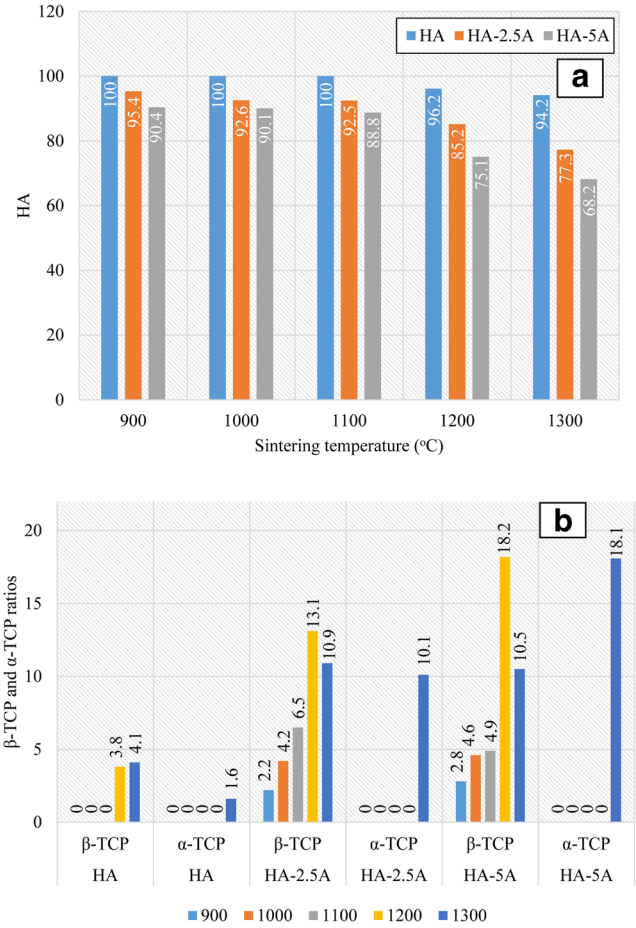

Fig. 8 Variation of **a** HA and **b** β-TCP and α-TCP ratios depending on the sintering temperatures in monolithic HA, HA–2.5A, and HA–5A

from 90.4 to 68.2% in HA–5A. The rate of change in HA ratios in the present study is in congruence with Evis [67].

Solid-state sintering of ceramic materials consists of three different stages, namely the formation of the neck, the elimination of open pores between the pelletized particles, and the elimination of the isolated pores in the grain boundaries by grain boundary diffusion. Various factors such as particle, ionic size, mixing ratio, chemical potential gradient, dwelling time, sintering temperature, and diffusion coefficients of the reacting species govern the product formation [68]. It is seen in Fig. 9 that porous structures due to insufficient sintering at temperatures of ≤ 1100 °C, in contrast to the dense structures at sintering temperatures of > 1100 °C and also the formation of microcracks at high temperatures, were observed. SEM images also revealed that regions have nonhomogeneous grain sizes as well as formed small grains between the overgrown grains and grain boundaries at certain sintering temperatures and compositions. It is thought that these small grains are related to the intermediate phases formed via solid-state reactions between HA and Al_2O_3 powders which had been detected by XRD analysis. As noted by Zyman et al. [69], these formations contribute to increased mechanical properties

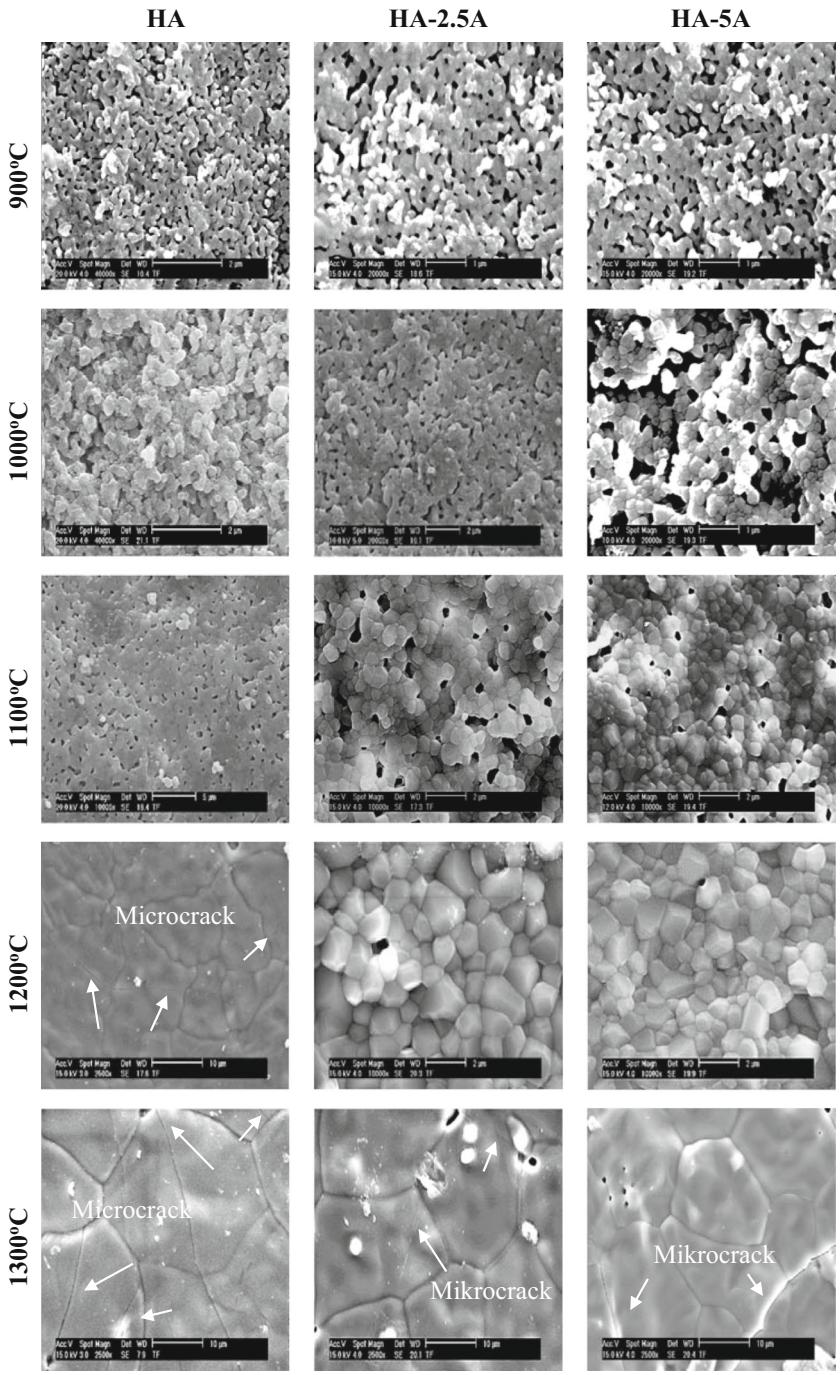

Fig. 9 SEM microstructure images of monolithic HA, HA–2.5A, and HA–5A samples depending on the sintering temperatures

because of the formation of strong intergranular bonds between the grains and the inhibition of growth in HA granules. Microcracks are caused by the different thermal expansion coefficients of detected phases such as HA, β-TCP, α-TCP, and calcium aluminate phases, which induce mechanical stresses in sintered samples during cooling from high temperatures to room temperature as stated in the literature [70]. Microcrack formations in polycrystalline ceramics do not occur when the average grain size values of the microstructure are below a certain critical value. HA has $P_{6/3m}$-type hexagonal crystal lattice structure and thermal expansion anisotropy. The thermal expansion anisotropy occurs due to the contraction or expansion of neighboring grains at different rates that depends on the crystallographic orientation in the microstructure [71]. From the SEM images in Fig. 9, it was determined that the average grain sizes increased by increasing sintering temperature. The average grain sizes of monolithic HA were determined to be 0.162 ± 0.019 μm at 900 °C, 0.186 ± 0.020 μm at 1000 °C, 0.473 ± 0.035 μm at 1100 °C, 7.955 ± 1.166 μm at 1200 °C, and 17.167 ± 2.156 μm at

1300 °C. The monolithic HA exhibits the formation of granules with homogeneous distribution at low temperatures; on the contrary, it exhibits a bimodal behavior when sintered at 1200 and 1300 °C as can be seen from the standard deviations. These differences in standard deviations for monolithic HA sintered at higher temperatures may be explained by the presence of second and/or third phases. The average grain sizes of the HA–2.5A binary composition are 0.113 ± 0.003, 0.238 ± 0.009, 0.384 ± 0.040, 0.858 ± 0.052, and 11.355 ± 3.542 μm, and they are 0.109 ± 0.014, 0.199 ± 0.019, 0.427 ± 0.033, 0.812 ± 0.110, and 10.171 ± 3.157 μm for HA–5A binary composition, respectively. As can be seen from these values, the addition of Al_2O_3 to HA caused the reduction in the average grain size of HA at about 32–40%, depending on the sintering temperature.

Figure 10 shows the activation energy curves required for the variation of average grain size values of monolithic HA and HA–A binary composites depending on sintering temperatures. The activation energy value of monolithic HA was determined to be 178.83 kJ/mol (42.56 kcal/mol). The activation energy value of the monolithic HA used in this study was determined to be compatible with some of the studies in the literature and lower and/or higher than the others. For example, it was determined as 29.16 kcal/mol [72], 35.13 kJ/mol [73], 40.15 kcal/mol [74], 44.00 kcal/mol [75], 48.50 kcal/mol [76], and 56.17 kcal/mol [77]. The reason for the lower and/or higher activation energy value of monolithic HA used in the present study compared to previous studies is related to its average particulate size and pressure for its pelletizing. As indicated by Ślósarczyk et al. [78], not only the increase in pelletizing pressure but also the decrease in particulate size causes the reduction in activation energy for grain growth. The activation energy of the HA–2.5A and HA–5A binary composites were found to be 176.79 kJ/mol (42.07 kcal/mol) and 173.95 kJ/mol (41.40 kcal/mol), respectively. As can be seen from these values, the activation energy values of the HA–A binary compounds were found to decrease with increasing Al_2O_3 ratio without causing grain growth. The reason why the activation energy value of HA–A binary composites are lower than monolithic HA is due to the inhibition of growth of the HA grains by calcium aluminate phases which were detected by XRD analysis. This situation had also been confirmed by Fanovich and L pez [79].

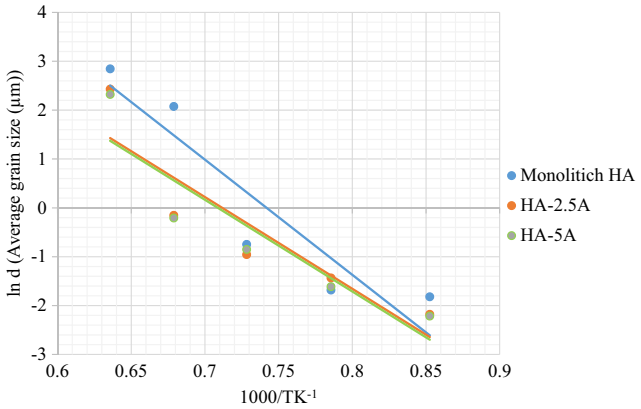

Fig. 10 Activation energy curve for monolithic HA, HA–2.5A, and HA–5A

Physical and mechanical properties of the sintered samples

Figure 11 shows the shrinkage ratios of the sintered samples. Shrinkage ratios of both monolithic HA and Al_2O_3-doped samples are increased by increasing sintering temperatures and change between 5 and 19%.

It has been found that the highest shrinkage ratios between temperatures of 900 and 1200 °C occur in monolithic HA. The shrinkage ratios of monolithic HA at these temperatures are 5.333 ± 0.571 (900 °C), 8.941 ± 0.383 (1000 °C), 13.534 ± 0.505 (1100 °C), and 17.734 ± 0.704 (1200 °C), respectively. For these temperatures, the shrinkage rates of HA–2.5A are 5.428 ± 0.249, 8.368 ± 0.336, 12.857 ± 0.440, and 17.731 ± 0.380%, while those of HA–5A are 5.312 ± 0.165, 7.478 ± 0.442, 12.031 ± 0.685, and 17.153 ± 0.365%, respectively. However, the highest shrinkage ratio at 1300 °C temperature belongs to the HA–2.5A composite with 18.301%. The shrinkage ratios at this temperature are 18.209 ± 0.622% for monolithic HA and 17.263 ± 0.751% for HA–5A, respectively. Furthermore, the shrinkage of HA–A binary composites decreases by increasing Al_2O_3 ratio for all sintering temperatures. As said by Zayman et al. [80], the gases, which formed by the movement of the moisture on the surface of HA powders between 20 and 500 °C and also of the moisture under the surface of the pelleted samples between 500 and 900 °C during the sintering of the HA ceramics, are trapped into closed porosities until the shrinkage is completed. While the size of the closed pores decreases with the sintering, the gas pressure in the closed pores increases. As a result of the increased gas pressure, the shrinkage slows down and the shrinkage is

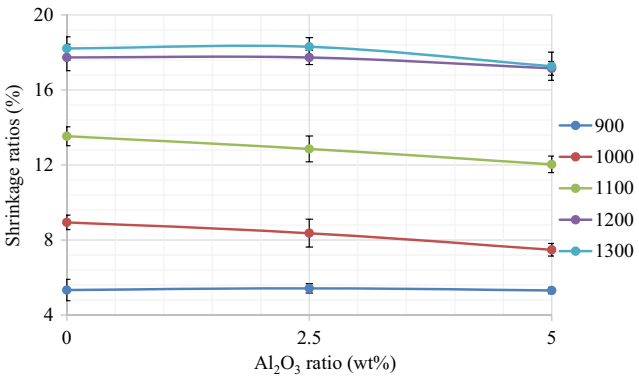

Fig. 11 Shrinkage ratios of HA and HA–Al_2O_3 binary composites depending on the sintering temperatures

completed if the gas pressure in the closed pores is greater than the capillary forces. In the present study, the shrinkage rates of monolithic HA, HA–2.5A, and HA–5A are completed at 18.20, 18.30, and 17.26%, respectively. Table 4 shows the green, theoretical, and relative density values before sintering for all groups. When Table 4 is examined, it is determined that the green density values are about 50%.

As can be seen in Fig. 12a, the porosity values of both monolithic HA and HA–A binary composites decreased with increasing sintering temperatures. Porosity values for monolithic HA were determined as 36.992 ± 0.500% at 900 °C, 31.396 ± 1.553% at 1000 °C, 26.589 ± 0.895% at 1100 °C, 4.018 ± 0.595% at 1200 °C, and 2.912 ± 0.769% at 1300 °C. The porosity values of HA–2.5A were 39.545 ± 0.373, 35.483 ± 1.405, 21.542 ± 1.138, 3.515 ± 0.313, and 2.533 ± 0.126%, while the porosity values of HA–5A were 39.475 ± 0.907, 33.277 ± 0.368, 21.044 ± 0.281, 3.324 ± 1.643, and 3.043 ± 0.685%, respectively. These values revealed that the porosity of monolithic HA can be reduced by the addition of Al_2O_3 powder from the sintering temperature of 900 °C. It is also seen that % porosity values of the HA–A binary compositions exhibit two different behaviors: first, it decreased with increasing Al_2O_3 ratio between 900 and 1100 °C; second, on the contrary, it increased with increasing Al_2O_3 content at 1200 and 1300 °C. As shown in Fig. 12b, the density values for both monolithic HA and HA–A binary composites increase by increasing sintering temperatures. The density of monolithic HA is attained to the highest value of 3.064 ± 0.024 g/cm^3, while it attained 3.032 ± 0.017 and 2.998 ± 0.028 g/cm^3 at 1300 °C. As seen in Fig. 12c, the relative density values of the sintered samples increase by increasing sintering temperature and it changes between 61.971 ± 0.376 and 98.353 ± 0.176% for monolithic HA, 59.753 ± 0.414 and 95.634 ± 0.541% for HA–2.5A, and 59.963 ± 0.692 and 94.053 ± 0.890% for HA–5A, respectively. The sintering contributed to the increase of the 50% partial density values of the pelletized samples over 94%. As stated by Champion et al. [81], the relative density value of monolithic HA ceramics which contains the TCP phase higher than 20% (β- and/or α-TCP) totally cannot exceed 90%. As seen in the XRD analysis of this study, as the total ratios of the β- and/or α-TCP phases of the monolithic HA are below 20%, the partial density values reached above 90%.

Porosity is important not only in terms of the improvement of mechanical properties but also the rate of binding with bone tissue of HA-based bioceramics [82]. Porous HA-based bioceramics are desirable to accelerate the growth of bone tissues, while dense HA bioceramics are preferred in applications where load bearing is required [83]. The densification of HA as a function of sintering temperature follows a sigmoidal correlation with the attainment of plateau densification levels at 1100–1300 °C. The plateau temperature and associated limiting densification level depend predominantly on the surface area of the HAp powder and to a lesser extent on the heating rate and Ca/P ratio [84]. There are three reasons why

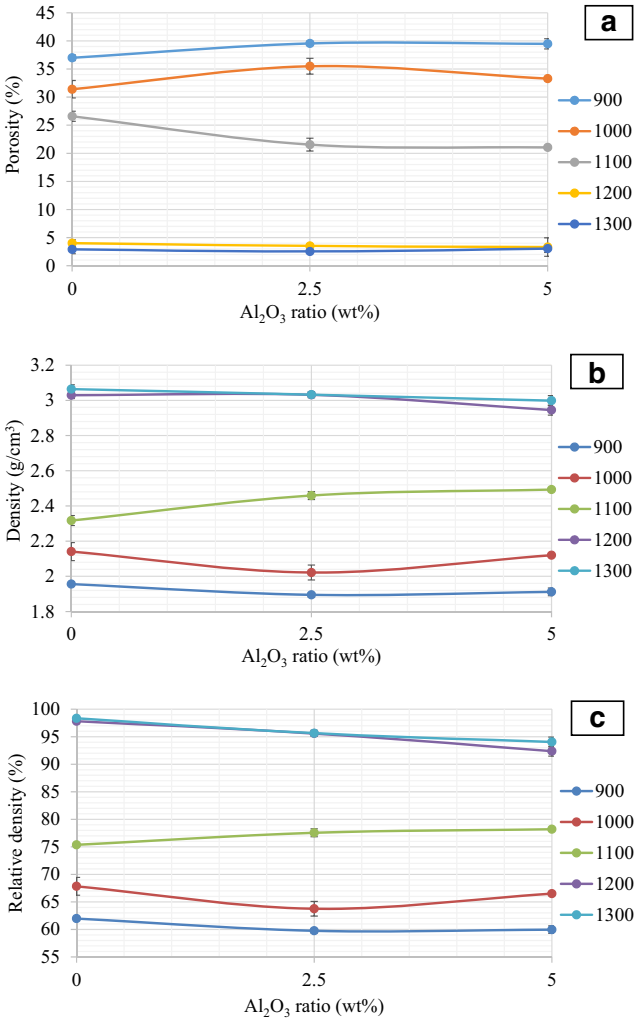

Fig. 12 **a** Porosity, **b** density, and **c** relative density values of monolithic HA, HA–2.5A, and HA–5A depending on the sintering temperatures

Table 4 The green, theoretical, and relative density values of the pelleted samples with and without Al_2O_3 addition

Sample ID	Green density (g/cm^3)	Theoretical density (g/cm^3)	Relative density of pelleted samples (%)
HA	1.651 ± 0.016	3.156	52.316 ± 0.529
HA–2.5A	1.648 ± 0.016	3.171	52.000 ± 0.522
HA–5A	1.659 ± 0.010	3.188	52.045 ± 0.580

the density values of the HA–A binary composites are lower or higher than the monolithic HA, which are as follows:

1. As the porosity ratios of HA–A binary composites are higher than monolithic HA in some temperatures.
2. Increase in the decomposition rates of HA to β-TCP and α-TCP, which have lower density values compared to HA, and in HA–A binary compounds compared to monolithic HA (HA 3.156 g/cm^3, β-TCP 3.07 g/cm^3 [85], α-TCP 2.86 g/cm^3 [86]).
3. In the intermediate phases, calcium aluminates, which occurred during solid-state sintering of HA and Al_2O_3 powders, have dissimilar theoretical density values ($Ca_3Al_2O_6 = 3.04$ g/cm^3, $CaAl_4O_7 = 2.91$ g/cm^3, $CaAl_2O_4 = 2.98$ g/cm^3, $Ca_5Al_6O_{14} = 3.03$ g/cm^3, $Ca_2Al_2O_5 = 3.73$ g/cm^3 [87]).

Densification around 90% is desirable because the presence of a certain degree of porosity (at about 10%), as well as of the absorbable phases (α- and β-TCP), contributes to bone intergrowth and to subsequent implant–bone interfacial adhesion [88]. It appears that this condition is specified by the XRD analysis, and the relative density values of this study are satisfied.

Hardness, H, and toughness, K_{IC}, are convenient material parameters for characterizing deformation and fracture phenomena in a large scale of solids ranging from metals to ceramics. The properties of HA powders such as surface area and grain size distribution affect the hardness and toughness properties of HA ceramics [89]. Furthermore, the hardness of unreinforced or reinforced HA ceramics changes depending on the method and conditions of sintering, ratio and sizes of porosity, the type and ratio of second phases, the average grain size of the sintered samples, and the type and amount of reinforcement material [90].

As stated in the literature, the values of the hardness of monolithic HA ceramics sintered up to 1300 °C temperature reached 4.8 GPa. In this study, it was determined that the highest microhardness values were 4.87 ± 0.15, 4.77 ± 0.27, and 4.62 ± 0.48 GPa for the monolithic HA, HA–2.5A, and HA–5A binary composites, respectively. The highest microhardness values for almost all sintering temperatures belong to the monolithic HA even if the microhardness values of HA–Al_2O_3 binary composites increase with increasing sintering temperatures, as seen in Fig. 13. The microhardness values of the HA–A binary composites generally reduced by increasing Al_2O_3 ratios. This decrease in microhardness values of the HA–A binary compositions is due to the melting point of Al_2O_3 being higher than that of HA [91].

Due to the low fracture toughness, monolithic HA cannot be used as a bioceramic where load bearing is required. Numerous studies were carried out in order to understand the effect of reinforcement of materials using different fracture toughness measurement methods on the fracture toughness of monolithic HA [92–95].

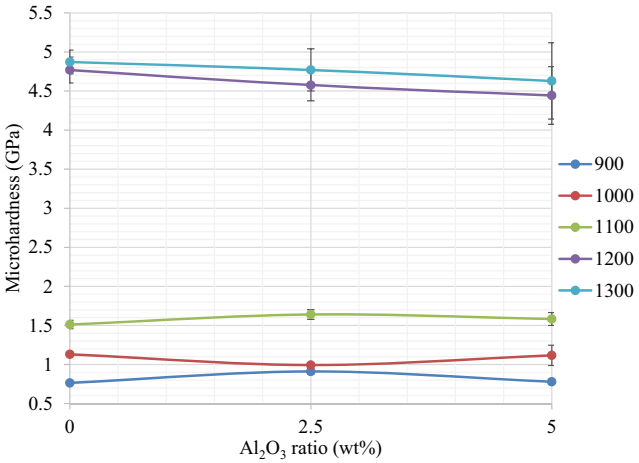

Fig. 13 Changes in microhardness values of monolithic HA and HA–Al_2O_3 composites depending on the sintering temperatures

As seen in Fig. 14, the K_{IC} values of monolithic HA increased with increasing sintering temperatures until 1100 °C and reached the highest value of 0.96 ± 0.05 MPa m$^{1/2}$, but drastically decreased with increasing sintering temperatures. The K_{IC} values of monolithic HA were measured as 0.92 ± 0.06 and 0.71 ± 0.13 MPa m$^{1/2}$ at 1200 and 1300 °C, respectively. Although there is an increase in the density value of monolithic HA at these temperatures, there are three main reasons for the reduction in fracture toughness values: (i) the decrease in the number of grains that will prevent the progress of cracks with increasing grain size, (ii) transgranular progression of cracks rather than intergranular, and (iii) formation of residual stresses in the sintered samples at elevated temperatures due to the decomposition of HA [96, 97]. The low fracture toughness of monolithic HA ceramics can be increased by the inhibition of the grain growth of HA and/or cause the formation of larger energies during crack progression which allow cracks to progress intergranularly instead of transgranularly [98]. When the fracture toughness values of

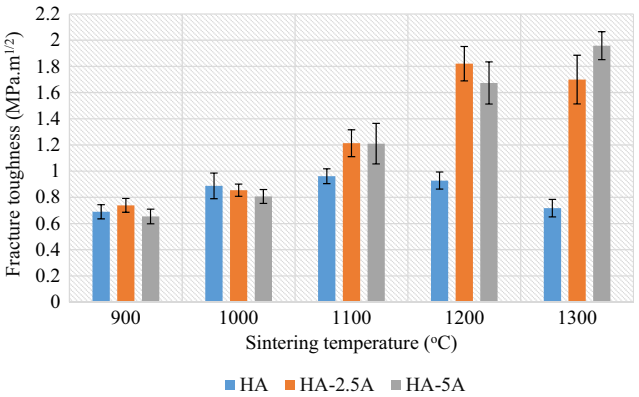

Fig. 14 Changes in fracture toughness values of monolithic HA and HA–A binary composites depending on the sintering temperatures

HA–A binary composites are examined depending on the sintering temperatures and Al_2O_3 ratios, it was determined that the K_{IC} values of the HA–2.5A binary composition increased to 1200 °C and reached the highest value of 1.82 ± 0.13 MPa $m^{1/2}$ and decreased to 1.69 ± 0.18 MPa $m^{1/2}$ at 1300 °C. Furthermore, the K_{IC} values of the HA–5A binary composition increased up to 1300 °C and reached 1.95 ± 0.10 MPa $m^{1/2}$. It is seen from these values that the K_{IC} value of monolithic HA can be increased up to about 2 times by the addition of Al_2O_3 to HA. These values of the HA–A binary composites are compatible with the literature (30 vol% Al_2O_3–HA, about 2.0 MPa $m^{1/2}$) [99]. Because of the lower grain size and the more porous microstructure which prevents the progress of the crack, the K_{IC} value of HA–5A is higher than HA–2.5A.

As a structural material, HA is a very brittle ceramic which is strong in compression and weak in tension [100]. Depending on the starting particulate size, type and number of impurities, pelletizing pressure, sintering atmosphere, and sintering temperatures and regime, the compressive strength of commercially available HA ranges from 200 to 918 MPa [101].

Figure 15 shows the compressive strength of the sintered samples. It was determined that the compressive strength of monolithic HA attained the maximum value of 130 ± 6.22 MPa until 1100 °C, but it decreased to 101.8 ± 5.01 and 65.6 ± 5.59 MPa at elevated temperatures in which it contains the second and/or third phases such as β- and/or α-TCP and CaO. Figure 15 reveals that the maximum compressive strength of 130 ± 6.22 MPa (1100 °C) cannot be obtained, even if the maximum densification is completed at elevated temperatures. It has also been found in the literature that a similar trend occurred in previous studies. For example, Vallet-Regí et al. [102] found that the maximum compressive strength value of 700 MPa was obtained at 1100 °C and it decreased to 350 MPa even if the densification rate was about 96% at 1300 °C. When the compressive strength values of HA–Al_2O_3 binary composites were examined, it was found that the compressive strength of monolithic HA could be increased at almost all sintering temperatures by the addition of Al_2O_3 to HA. In addition to that, Fig. 15 also reveals that the compressive strength for HA–2.5A and HA–5A reached the maximum value of 182.75 ± 28.14 and 214 ± 32.50 MPa, respectively. These values are higher than the compressive strength of monolithic HA at about 79.54 and 111%. However, the compressive strength values of HA–A binary composites sintered at 1300 °C decreased compared to those at 1200 °C. It was determined that HA–Al_2O_3 binary compositions ($\sigma_{HA-2.5A}$ = 153 ± 28.1 MPa, σ_{HA-5A} = 149.7 ± 32.8 MPa) had higher compressive strength values than monolithic HA for this temperature. The highest compressive strength value of 214 MPa obtained in the present study is compatible with the study prepared by Hannora, who had found 230 MPa [103]. In that study, Hannora had added Al_2O_3 to HA at 15 wt%. In order to achieve the higher densification ratio in HA ceramics, high temperature and long sintering times are required in the pressureless sintering process. However, this leads to excessive grain growth in HA ceramics, increase in the rate of decomposition, and decrease in mechanical properties [104]. Due to these reasons, it is thought that the compressive strength values of HA–A composites sintered at 1300 °C and monolithic HA sintered at 1200 and 1300 °C are decreasing.

Figure 16 shows the three-point bending strength of the sintered samples. While the three-point bending strength of unreinforced and zero porosity HA ceramics is about 112 MPa, it decreases to 33.9 MPa depending on the porosity ratio as stated by Umakoshi et al. [105] and Suwanprateeb et al. [106]. The bending strength of the monolithic HA begins to increase from the sintering temperature of 900 °C (27.7 ± 6.34 MPa), and it reaches the maximum value of 60.27 ± 9.93 MPa at 1100 °C and finally decreases with increasing

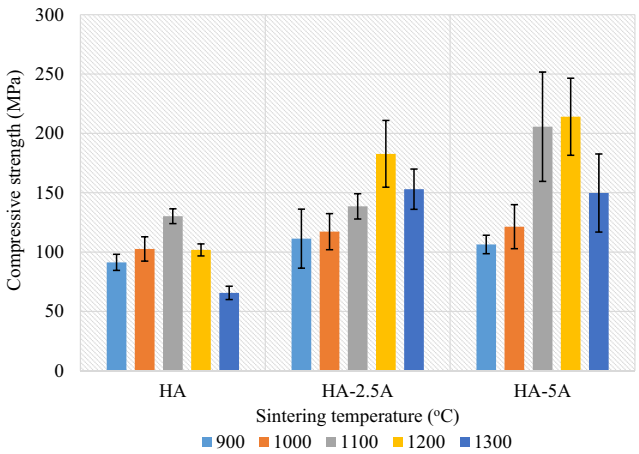

Fig. 15 Compressive strength values of the monolithic HA, HA–2.5A, and HA–5A depending on the sintering temperatures

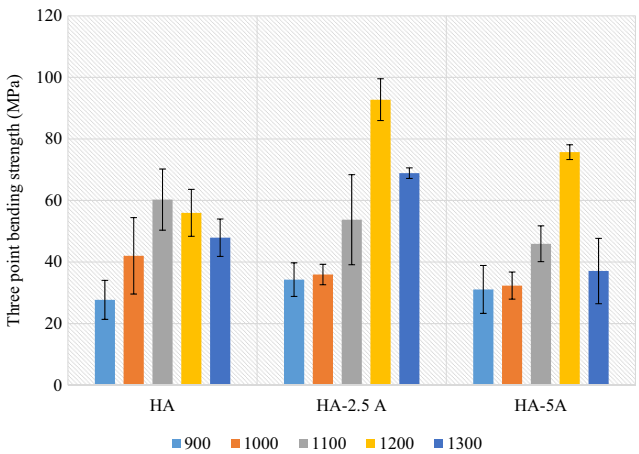

Fig. 16 Three-point bending strengths of monolithic HA, HA–2.5A, and HA–5A composites

sintering temperatures as in the measurements of fracture toughness and compressive strength. The highest three-point bending value of monolithic HA is compatible with the values of 57.4 MPa [107], 61 MPa [108], and 69.5 MPa [109]. However, it was found to have a higher ratio than 43 MPa obtained by Juang and Hon [110] and to have a lower ratio than 84.6 MPa obtained by Jiang et al. [111]. The reason for the incompatibility with these studies is due to the difference in the test conditions, sample sizes, pelletizing pressures, and method. Although the three-point bending strengths of the HA–A binary composites decrease at all sintering temperatures due to the increase in Al_2O_3 ratio, it attained 98.87 ± 6.78 MPa for HA–2.5A and 75.70 ± 2.40 MPa for HA–5A at 1200 °C and then decreased to the values of 68.87 ± 1.70 and 37.07 ± 10.62 MPa at 1300 °C, respectively. The three-point bending strengths of HA–A composites are higher than monolithic HA related to the grain growth inhibition by Al_2O_3 additives.

In vitro bioactivity properties

It is well known that the in vitro test can be performed for the evaluation of the bioactivity properties of the materials which will be used as a biomaterial in the human body; on the other hand, it is cheaper and it requires a short time to complete compared to in vivo testing. Figures 17 and 18 show the SEM images of the samples immersed into SBF solution.

As shown in Fig. 17a, the apatite crystals started forming in cubic shape at the end of a short immersing period like 3 days. After 7 days of immersing into SBF solution, it was observed that apatite crystals begin to grow in dendritic form instead of cubic shape. The size and thickness of dendritic apatite layers increased in 15 days. After 30 days of immersion, the surface of the samples showed highly dense apatite layers. The crack-like regions that formed along the interfaces of the apatite layers after 30 days of immersing time are drying cracks [112]. As a result of the SBF analysis, monolithic HA used as a matrix material was found to have a biocompatible structure as it allows the formation of apatite layers on the surface. The ratio and the amount of apatite occurrence on the surface of the immersed samples increased by increasing times.

In vitro evaluation of the HA–5A binary composite shown in Fig. 18 revealed that the apatite layers growing in dendritic form in 7 days for monolithic HA appeared in 15 days for HA–A composition. It has been determined that apatite layers formed during 3 and 7 days occur at lower growth rates for the HA–A composite than monolithic HA. It was observed that the apatite layers formed after 30 days of waiting time covered the entire surface as it was in the monolithic HA. This means that the alumina, which has a bioinert structure, causes a slight decrease in the biocompatibility of HA. But compared to

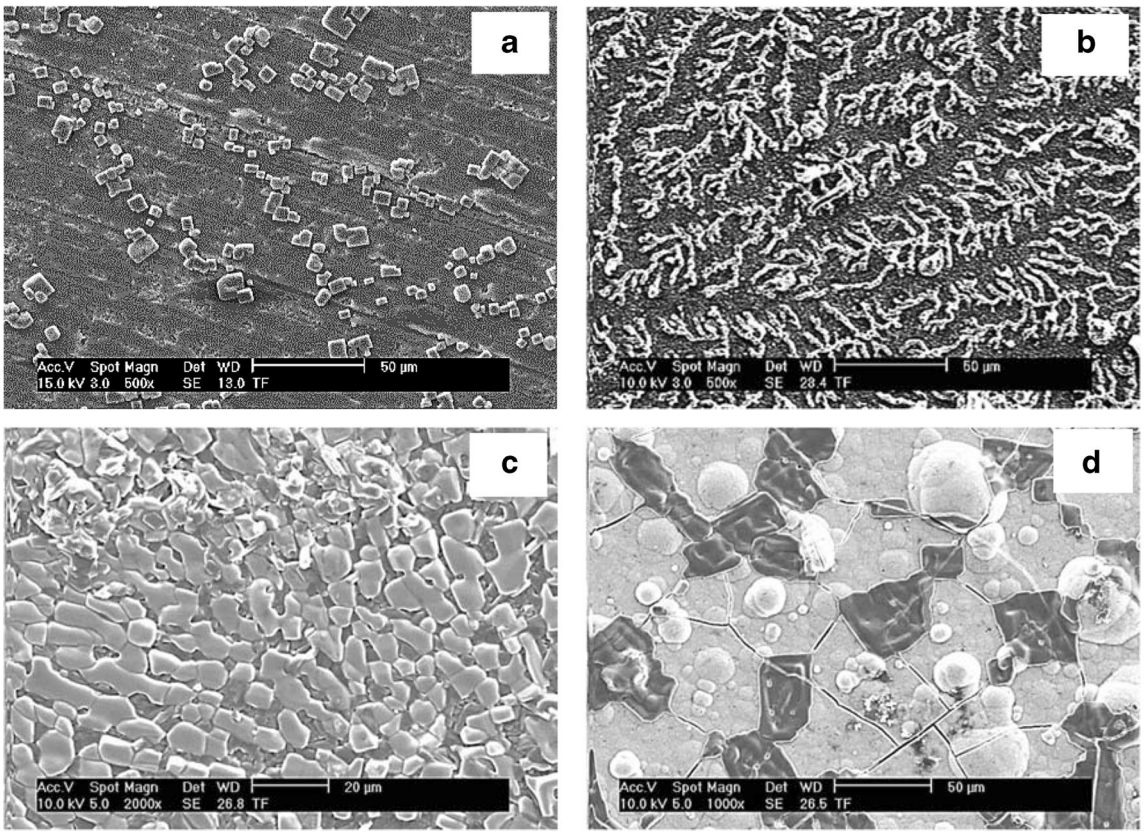

Fig. 17 SEM images of the apatite layers on the surface of monolithic HA after immersing into the SBF solution **a** 3, **b** 7, **c** 15, and **d** 30 days

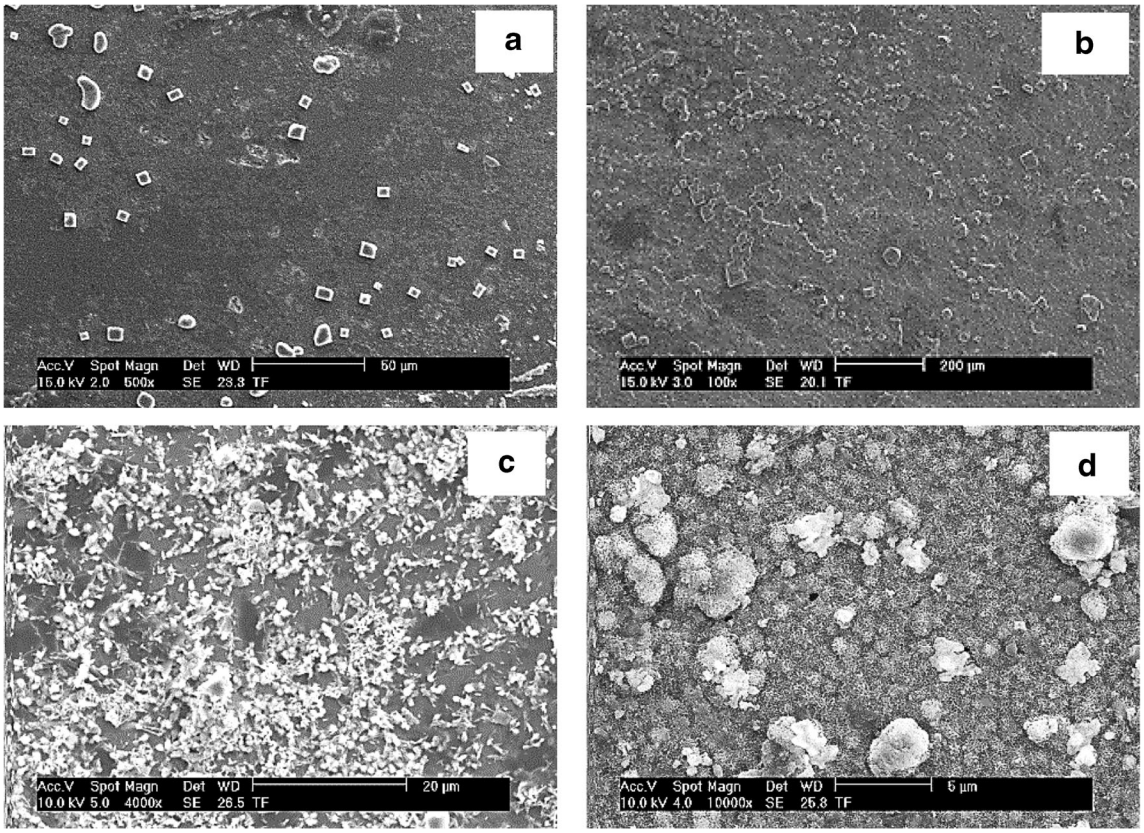

Fig. 18 SEM images of the apatite layers on the surface of HA–5A composite after immersing into the SBF solution for **a** 3, **b** 7, **c** 15, and **d** 30 days

previous studies, the in vitro bioactivity of the HA–A composite in the present study is higher than that of the other composites [17, 113]. This is because the Al_2O_3 ratios used in other studies are higher than in the present study. The biological behavior of HA ceramics varies depending on the preparation method of HA powders, chemical composition, and surface properties such as bulk HA ceramic production conditions and topography, roughness, surface energy, and wettability [114, 115]. Another calcium phosphate compound, β-TCP, slowly dissolves compared to α-TCP when it is implanted in the human body, and when it completely resolves, it contributes to the formation of new bone tissues, so it can be used in the human body. However, β-TCP is not suitable for long-term use in the human body since it has 3 to 12 times higher solubility than HA [116]. Another calcium phosphate compound, α-TCP, is not appropriate to use as a biomaterial since its solubility is higher than that of β-TCP [117]. The coexistence of HA and β-TCP phases at specific ratios is particularly important in order to be able to bind with bone and for rapid healing [118]. The coexistence of HA with β-TCP has been found to contribute to the formation of bone tissue at a higher rate than using pure HA [119]. It was reported that the presence of CaO in an implant material is so harmful due to its high reactivity against water. Moreover, the existence of CaO would cause decohesion of the material, due to stresses arising from the formation of $Ca(OH)_2$ and related volume changes [120–122]. The CaO phase, which was determined to be formed in addition to β-TCP and α-TCP as a result of the sintering of the monolithic HA at 1300 °C, had not been detected by XRD analysis and neither was the monolithic HA or HA–5A composite before testing of SBF in vitro bioactivity. Because of this reason, it is considered that both monolithic HA and HA–5A binary compound have usable quality in the human body.

Conclusion

HA powder decomposed at above 1100 °C and its mechanical properties decreased just before densification had completed. The highest mechanical strengths were obtained for HA without Al_2O_3 additive, when it was sintered at 1100 °C. Although the addition of Al_2O_3 leads to increment in the decomposition ratio, the main phase was HA for all the sintered samples. While the decomposition ratio was less than 5% for monolithic HA, it attained 22.7 and 31.8% for HA–2.5A and HA–5A composites, respectively. The growth of HA grains was inhibited by the addition of Al_2O_3. For this reason, all the mechanical properties of monolithic HA except hardness and densification rate were improved, higher than the rate of 60%. Microcracks due to dissimilar thermal expansion coefficient of β-TCP, α-TCP, and calcium aluminate phases were

observed for HA–Al_2O_3 samples. Although the addition of Al_2O_3 leads to the reduction of the in vitro bioactivity of HA, the absence of CaO phase in the samples subjected to the in vitro testing indicated that the materials are usable in the human body.

Funding information The authors thank the economic support of the Scientific Research Centre of Marmara University (Project No: FEN-A-100616-0272).

References

1. Hench, L.L.: Medical materials for the next millennium. MRS Bull. **24**(5), 13–20 (1999)
2. Kamitakahara, M., Ohtsuki, C., Miyazaki, T.: Review paper: Behavior of ceramic biomaterials derived from tricalcium phosphate in physiological condition. J. Biomater. Appl. **23**, 197–212 (2008)
3. Bellucci, D., Desogus, L., Montinaro, S., Orrù, R., Cao, G., Cannillo, V.: Innovative hydroxyapatite/bioactive glass composites processed by spark plasma sintering for bone tissue repair. J. Eur. Ceram. Soc. **37**, 1723–1733 (2017)
4. Prokopiev, O., Sevostianov, I.: Dependence of the mechanical properties of sintered hydroxyapatite on the sintering temperature. Mater. Sci. Eng. A. **431**, 218–227 (2006)
5. Uysal, I., Severcan, F., Tezcaner, A., Evis, Z.: Co-doping of hydroxyapatite with zinc and fluoride improves mechanical and biological properties of hydroxyapatite. Prog. Nat. Sci.: Mater. Int. **24**, 340–349 (2014)
6. Ramesh, S., Natasha, A.N., Tan, C.Y., Bang, L.T., Ramesh, S., Ching, C.Y., Chandran, H.: Direct conversion of eggshell to hydroxyapatite ceramic by a sintering method. Ceram. Int. **42**, 7824–7829 (2016)
7. Metsger, D.S., Rieger, M.R., Foreman, D.W.: Mechanical properties of sintered hydroxyapatite and tricalcium phosphate ceramics. J. Mater. Sci. Mater. Med. **10**, 9–17 (1999)
8. Oktar, F.N., Göller, G.: Sintering effects on mechanical properties of glass-reinforced hydroxyapatite composites. Ceram. Int. **28**, 617–621 (2002)
9. Mobasherpour, I., Hashjin, M.S., Toosi, S.S.R., Kamachali, R.D.: Effect of the addition ZrO_2-Al_2O_3 on nanocrystalline hydroxyapatite bending strength and fracture toughness. Ceram. Int. **35**, 1569–1574 (2009)
10. Lee, K.T., Cha, S.I., Kim, K.T., Lee, K.H., Hong, S.H.: Sintering behavior, microstructural evolution, and mechanical properties of ultra-fine grained alumina synthesized via in-situ spark plasma sintering. Ceram. Int. **42**, 4290–4297 (2016)
11. Halim, T., Burgett-Moreno, M., Donaldson, T., Clarke, I.C.: Third-body wear damage produced in CoCr surfaces by hydroxyapatite and alumina ceramic debris: a 10-cycle metal-on-metal simulator study. Reconstr. Rev. **5**(4), 33–39 (2015)
12. Berger, J., Roch, T., Pistillo, N., Lasagni, A.F.: Multiple-beam laser patterning on aluminum oxide, zirconium oxide, and hydroxyapatite ceramic materials using a microlens array. J. Laser Appl. **28**(4), 042003-1–042003-8 (2016)
13. Kim, C.Y., Jee, S.S.: Hydroxyapatite formation on bioactive-glazed alumina. J. Eur. Ceram. Soc. **23**, 1803–1811 (2003)
14. Acchar, W., Cairo, C.A.: The influence of (Ti,W)C and NbC on the mechanical behavior of alumina. Mater. Res. **9**(2), 171–174 (2006)
15. Ibrahim, M.Z., Sarhan, A.A.D., Yusuf, F., Hamdi, M.: Biomedical materials and techniques to improve the tribological, mechanical and biomedical properties of orthopedic implants. J. Alloys Compd. **714**, 636–667 (2017)
16. Bandyopadhyay, A., Bernard, S., Xue, W., Bose, S.: Calcium phosphate-based resorbable ceramics: influence of MgO, ZnO, and SiO_2 dopants. J. Am. Ceram. Soc. **89**(9), 2675–2688 (2006)
17. Kalmodia, S., Goenka, S., Laha, T., Lahiri, D., Basu, B., Balani, K.: Microstructure, mechanical properties, and in vitro biocompatibility of spark plasma sintered hydroxyapatite-aluminum oxide-carbon nanotube composite. Mater. Sci. Eng. C. **30**, 1162–1169 (2010)
18. Jun, Y.K., Kim, W.H., Kweon, O.K., Hong, S.H.: The fabrication and biochemical evaluation of alumina reinforced calcium phosphate porous implants. Biomaterials. **24**, 3731–3739 (2003)
19. Fujita, H., Kudo, T., Kanetaka, H., Miyazaki, T., Hashimoto, M., Kawashita, M.: Adsorption of laminin on hydroxyapatite and alumina and the MC3T3-E1 cell response. ACS Biomater. Sci. Eng. **2**, 1162–1168 (2016)
20. ASTM F 1185-88 (1993). Standard Specification for Composition of Ceramic Hydroxylapatite for Surgical Implants, American Society for Testing and Materials, Conshohocken
21. Landi, E., Tampieri, A., Celotti, G., Sprio, S., Sandri, M., Logroscino, G.: Sr-substituted hydroxyapatites for osteoporotic bone replacement. Acta Biomater. **3**, 961–969 (2007)
22. Ha, J.S.: Fabrication and characterization of hydroxyapatite/mullite and tricalcium phosphate/Al_2O_3 composites containing 30 wt% of bioactive components. J. Korean Ceram. Soc. **52**(5), 374–379 (2015)
23. Ji, H., Marquis, P.M.: Preparation and characterization of Al_2O_3 reinforced hydroxyapatite. Biomaterials. **13**, 744–748 (1992)
24. British Standard Non-Metallic Materials for Surgical Implants. Part 2: Specifications for Ceramic Materials Based on Alumina, BS 7253: Part 2: 1990 ISO 6474-1981
25. Sato, K., Yugami, H., Hashida, T.: Effect of rare-earth oxides on fracture properties of ceria ceramics. J. Mater. Sci. **39**, 5765–5770 (2004)
26. Muralithran, G., Ramesh, S.: The effects of sintering temperature on the properties of hydroxyapatite. Ceram. Int. **26**, 221–230 (2000)
27. Majling, J., Znáik, P., Palová, A., Stevīk, S., Kovalīk, S., Agrawal, D.K., Roy, R.: Sintering of the ultrahigh pressure densified hydroxyapatite monolithic xerogels. J. Mater. Res. **12**(1), 198–202 (1997)
28. Rahimiana, M., Ehsani, N., Parvin, N., Reza Baharvandi, H.: The effect of particle size, sintering temperature and sintering time on the properties of Al-Al_2O_3 composites, made by powder metallurgy. J. Mater. Process. Technol. **209**, 5387–5393 (2009)
29. Niihara, K.: Indentation microfracture of ceramics—its application and problems. J. Ceram. Soc. Jpn. **20**, 12–18 (1985)
30. ASTM C1161-94: Standard Test Method for Flexural Strength of Advanced Ceramics at Ambient Temperature. Annual Book of ASTM Standards, USA (1996)
31. Kokubo, T., Yamamuro, T., Hench, L.L., Wilson, J.: Handbook on Bioactive Ceramics: Bioactive Glasses and Glass-Ceramics, vol. 1. CRC, Boca Raton (1990)
32. Senamaud, N., Bemache-Assollant, D., Champion, E., Heughebaert, M., Rey, C.: Calcination and sintering of hydroxyfluorapatite powders. Solid State Ionics. **101-103**, 1357–1362 (1997)
33. Dorozhkin, S.V.: Multiphasic calcium orthophosphate ($CaPO_4$) bioceramics and their biomedical applications. Ceram. Int. **42**, 6529–6554 (2016)
34. Safina, M.N., Safronova, T.V., Lukin, E.S.: Calcium phosphate based ceramic with a resorbable phase and low sintering temperature. Glas. Ceram. **64**(7–8), 238–243 (2007)
35. Medveckỳ, Ľ., Štulajterova, R., Briančin, J.: Study of controlled tetracycline release from porous calcium phosphate/

polyhydroxybutyrate composites. Chem. Pap. **61**(6), 477–484 (2007)
36. Barros, B.S., de Oliveira, R.S., Kulesza, J., Melo, V.R.M., Melo, D.M.A., Alves, S.: $Ca_{3-x}Al_2O_6$:xEu^{3+} nanophosphors: fast synthesis and photophysical properties. J. Phys. Chem. Solids. **78**, 90–94 (2015)
37. Zhang, D., Pan, X., Yu, H., Zhai, Y.: Mineral transition of calcium aluminate clinker during high-temperature sintering with low-lime dosage. J. Mater. Sci. Technol. **31**, 1244–1250 (2015)
38. Mercury, J.M.R., de Aza, A.H., Pena, P.: Synthesis of $CaAl_2O_4$ from powders: particle size effect. J. Eur. Ceram. Soc. **25**, 3269–3279 (2005)
39. de Oliveira, I.R., de Andrade, T.L., Parreira, R.M., Jacobovitz, M., Pandolfelli, V.C.: Characterization of calcium aluminate cement phases when in contact with simulated body fluid. Mater. Res. **18**(2), 382–389 (2015)
40. Yuan, X., Xu, Y.B., He, Y.: Synthesis of $Ca_3Al_2O_6$ via citric acid precursor. Mater. Sci. Eng. A. **447**, 142–145 (2007)
41. Steele, F.A., Davey, W.P.: The crystal structure of tricalcium aluminate. J. Am. Chem. Soc. **51**(8), 2283–2293 (1929)
42. Mondal, P., Jeffery, J.W.: The crystal structure of tricalcium aluminate, $Ca_3Al_2O_6$. Acta Crystallogr. B. **31**, 689–697 (1975)
43. Liu, W., Chang, J.: Setting properties and biocompability of dicalcium silicate with varying additions of tricalcium aluminate. J. Biomater. Appl. **27**(2), 171–178 (2011)
44. Yuan, X., Xu, Y., He, Y.: Synthesis of $CaAl_4O_7$ via citric acid precursor. J. Alloys Compd. **441**, 251–254 (2007)
45. Suzuki, Y., Ohji, T.: Anisotropic thermal expansion of calcium dialuminate ($CaAl_4O_7$) simulated by molecular dynamics. Ceram. Int. **30**, 57–61 (2004)
46. Palchesko, R.N., McGowan, K.A., Gawalt, E.S.: Surface immobilization of active vancomycin on calcium aluminum oxide. Mater. Sci. Eng. C. **31**, 637–642 (2011)
47. Palchesko, R.N., Buckholtz, G.A., Romeo, J.D., Gawalt, E.S.: Co-immobilization of active antibiotics and cell adhesion peptides on calcium based biomaterials. Mater. Sci. Eng. C. **40**, 398–406 (2014)
48. Lazic, B., Krüger, H., Kahlenberg, V., Konzett, J., Kaindl, R.: Incommensurate structure of $Ca_2Al_2O_5$ at high temperatures—structure investigation and Raman spectroscopy. Acta Crystallogr. B. **64**(4), 417–425 (2008)
49. Kahlenberg, V., Fischer, R.X., Shaw, C.S.J.: Rietveld analysis of dicalcium aluminate ($Ca_2Al_2O_5$)—a new high pressure phase with the Brownmillerite-type structure. Am. Mineral. **85**, 1061–1065 (2000)
50. Kojitani, H., Wakabayashi, Y., Tejima, Y., Kato, C., Haraguchi, M., Akaogi, M.: High-pressure phase relations in $Ca_2AlSiO_{5.5}$ and energetics of perovskite-related compounds with oxygen defects in the $Ca_2Si_2O_6$–$Ca_2Al_2O_5$ join. Phys. Earth Planet. Inter. **173**, 349–353 (2009)
51. Guidara, A., Chaari, K., Bouaziz, J.: Elaboration and characterization of alumina-fluorapatite composites. J. Biomater. Nanobiotechnol. **2**, 103–113 (2011)
52. Xu, P., Zhou, Z., Zhao, C., Cheng, Z.: Catalytic performance of Ni/CaO-$Ca_5Al_6O_{14}$ bifunctional catalyst extrudate in sorption-enhanced steam methane reforming. Catal. Today. **259**, 347–353 (2016)
53. Chen, X., Yang, L., Zhou, Z., Cheng, Z.: Core-shell structured CaO-$Ca_9Al_6O_{18}$@$Ca_5Al_6O_{14}$/Ni bifunctional material for sorption-enhanced steam methane reforming. Chem. Eng. Sci. **163**, 114–122 (2017)
54. Cao, R., Zhang, F., Cao, C., Yu, X., Liang, A., Guo, S., Xue, H.: Synthesis and luminescence properties of $CaAl_2O_4$:Mn^{4+} phosphor. Opt. Mater. **38**, 53–56 (2014)
55. Cui, T., Ma, P., Sheng, Y., Zheng, K., Zhou, X., Xu, C., Zou, H., Song, Y.: Preparation of $CaAl_2O_4$:Eu^{2+}, Nd^{3+} and $SrAl_2O_4$:Eu^{2+}, Dy^{3+} long after glow luminescent materials using oil shale ash. Opt. Mater. **67**, 84–90 (2017)
56. Szczerba, J., Madej, D., Śniezek, E., Prorok, R.: The application of DTA and TG methods to investigate the non-crystalline hydration products of $CaAl_2O_4$ and $Ca_7ZrAl_6O_{18}$ compounds. Thermochim. Acta. **567**, 40–45 (2013)
57. Rodríguez, M.A., Aguilar, C.L., Aghayan, M.A.: Solution combustion synthesis and sintering behavior of $CaAl_2O_4$. Ceram. Int. **38**, 395–399 (2012)
58. Iftekhar, S., Grins, J., Svensson, G., Lööf, J., Jarmar, T., Botton, G.A., Andrei, C.M., Engqvist, H.: Phase formation of $CaAl_2O_4$ from $CaCO_3$-Al_2O_3 powder mixtures. J. Eur. Ceram. Soc. **28**, 747–756 (2008)
59. Kumar, P.N., Ferreira, J.M.F., Kannan, S.: Phase transition mechanisms involved in the formation of structurally stable β-$Ca_3(PO_4)_2$-α-Al_2O_3 composites. J. Eur. Ceram. Soc. **37**, 2953–2963 (2017)
60. Lööf, J., Svahn, F., Jarmar, T., Engqvist, H., Pameijer, C.H.: A comparative study of the bioactivity of three materials for dental applications. Dent. Mater. **24**, 653–659 (2008)
61. Acuña-Gutiérrez, I.O., Escobedo-Bocardo, J.C., Almanza-Robles, J.M., Cortés-Hernández, D.A., Saldívar-Ramírez, M.M.G., Reséndiz-Hernández, P.J., Zugasti-Cruz, A.: Development of LiCl-containing calcium aluminate cement for bone repair and remodeling applications. Mater. Sci. Eng. C. **70**, 357–363 (2017)
62. Viswanath, B., Ravishankar, N.: Interfacial reactions in hydroxyapatite/alumina nanocomposites. Scr. Mater. **55**, 863–866 (2006)
63. Evis, Z., Doremus, R.H.: Effect of AlF_3, CaF_2 and MgF_2 on hot-pressed hydroxyapatite-nanophase alpha-alumina composites. Mater. Res. Bull. **43**, 2643–2651 (2008)
64. Zhang, C., Zhang, X., Liu, C., Sun, K., Yuan, J.: Nano-alumina/hydroxyapatite composite powders prepared by in-situ chemical precipitation. Ceram. Int. **42**, 279–285 (2016)
65. Radha, G., Balakumar, S., Venkatesan, B., Vellaichamy, E.: Evaluation of hemocompatibility and in vitro immersion on microwave-assisted hydroxyapatite-alumina nanocomposites. Mater. Sci. Eng. C. **50**, 143–150 (2015)
66. Epure, L.M., Dimitrievska, S., Merhi, Y., Yahia, L.H.: The effect of varying Al_2O_3 percentage in hydroxyapatite/Al_2O_3 composite materials: morphological, chemical and cytotoxic evaluation. J. Biomed. Mater. Res. A. **83A**(4), 1009–1023 (2007)
67. Evis, Z.: Al^{+3} doped nano-hydroxyapatites and their sintering characteristics. J. Ceram. Soc. Jpn. **114**(11), 1001–1004 (2006)
68. Ali, M.M., Agarwaland, S.K., Handoo, S.K.: Diffusion studies information and sintering of $CaAl_2O_4$ and $BaAl_2O_4$: a comparative evaluation. Cem. Concr. Res. **27**(7), 979–982 (1997)
69. Zyman, Z., Tkachenko, M., Epple, M., Polyakov, M., Naboka, M.: Magnesium-substituted hydroxyapatite ceramics. Mater. Werkst. **37**(6), 474–477 (2006)
70. Guo, H., Khor, K.A., Boey, Y.C., Miao, X.: Laminated and functionally graded hydroxyapatite/yttria stabilized tetragonal zirconia composites fabricated by spark plasma sintering. Biomaterials. **24**, 667–675 (2003)
71. Li, S., Izui, H., Okano, M.: Densification, microstructure, and behavior of hydroxyapatite ceramics sintered by using spark plasma sintering. J. Eng. Mater. Technol. **130**, 031012-1–031012-7 (2008)
72. Halouani, R., Bernache-Assolant, D., Champion, E., Ababou, A.: Microstructure and related mechanical properties of hot pressed hydroxyapatite ceramics. J. Mater. Sci. Mater. Med. **5**, 563–568 (1994)
73. Aizawa, M., Hanazawa, T., Itatani, K., Howell, F.S., Kishioka, A.: Characterization of hydroxyapatite powders prepared by ultrasonic spray-pyrolysis technique. J. Mater. Sci. **34**, 2865–2873 (1992)

74. Yoshida, H., Kim, B.N., Son, H.W., Han, Y.H., Kim, S.: Superplastic deformation of transparent hydroxyapatite. Scr. Mater. **69**, 155–158 (2013)
75. Gu, Y.W., Loh, N.H., Khor, K.A., Tor, S.B., Cheang, P.: Spark plasma sintering of hydroxyapatite powders. Biomaterials. **23**, 37–43 (2002)
76. Lopes, M.A., Monteiro, F.J., Santos, J.D.: Glass-reinforced hydroxyapatite composites: secondary phase proportions and densification effects on biaxial bending strength. J. Biomed. Mater. Res. A. **48**(5), 734–740 (1999)
77. Wang, T., Dorner-Reisel, A., Müller, E.: Thermogravimetric and thermokinetic investigation of the dehydroxylation of a hydroxyapatite powder. J. Eur. Ceram. Soc. **24**, 693–698 (2004)
78. Ślósarczyk, A., Klisch, M., Błaẑewicz, M., Piekarczyk, J., Stobierski, L., Rapacz-Kmita, A.: Hot pressed hydroxyapatite-carbon fibre composites. J. Eur. Ceram. Soc. **20**, 1397–1402 (2000)
79. Fanovich, M.A., L pez, J.M.P.: Influence of temperature and additives on the microstructure and sintering behaviour of hydroxyapatite with different Ca/P ratios. J. Mater. Sci. Mater. Med. **9**, 53–60 (1998)
80. Zayman, Z.Z., Ivanov, I.G., Glushko, V.I.: Possibilities for strengthening hydroxyapatite ceramics. J. Biomed. Mater. Res. **46**(1), 73–79 (1999)
81. Raynaud, S., Champion, E., Bernache-Assollant, D.: Calcium phosphate apatites with variable Ca/P atomic ratio II. Calcination and sintering. Biomaterials. **23**, 1073–1080 (2002)
82. Arita, I.H., Wilkinson, D.S., Mondragón, M.A., Castaño, V.M.: Chemistry and sintering behaviour of thin hydroxyapatite ceramics with controlled porosity. Biomaterials. **16**, 403–408 (1995)
83. Deville, S., Saiz, E., Tomsia, A.P.: Freeze casting of hydroxyapatite scaffolds for bone tissue engineering. Biomaterials. **27**, 5480–5489 (2006)
84. Ruys, A.J., Wei, M., Sorrell, C.C., Dickson, M.R., Brandwood, A., Milthorpe, B.K.: Sintering effects on the strength of hydroxyapatite. Biomaterials. **16**, 409–415 (1995)
85. Miao, X., Chen, Y., Guo, H., Khor, K.A.: Spark plasma sintered hydroxyapatite-yttria stabilized zirconia composites. Ceram. Int. **30**, 1793–1796 (2004)
86. Wang, X., Fan, H., Xiao, Y., Zhang, X.: Fabrication and characterization of porous hydroxyapatite/β-tricalcium phosphate ceramics by microwave sintering. Mater. Lett. **60**, 455–458 (2006)
87. Kahlenberg, V., Fischer, R.X., Shaw, C.S.J.: High-pressure $Ca_4Al_6O_{13}$: an example of a calcium aluminate with three different types of coordination polyhedra for aluminum. Am. Mineral. **85**, 1492–1496 (2000)
88. Silva, V.V., Lameiras, F.S., Domingues, R.Z.: Microstructural and mechanical study of zirconia-hydroxyapatite (ZH) composite ceramics for biomedical applications. Compos. Sci. Technol. **61**, 301–310 (2001)
89. Ślósarczyk, A., Białoskórski, J.: Hardness and fracture toughness of dense calcium-phosphate-based materials. J. Mater. Sci. Mater. Med. **9**, 103–108 (1998)
90. Hoepfner, T.P., Case, E.D.: The influence of the microstructure on the hardness of sintered hydroxyapatite. Ceram. Int. **29**, 699–706 (2003)
91. Chiba, A., Kimura, S., Raghukandan, K., Morizono, Y.: Effect of alumina addition on hydroxyapatite biocomposites fabricated by underwater-shock compaction. Mater. Sci. Eng. A. **350**, 179–183 (2003)
92. Lee, B.T., Shin, N.Y., Han, J.K., Song, H.Y.: Microstructures and fracture characteristics of spark plasma-sintered Hap-5 vol.% Ag composites. Mater. Sci. Eng. A. **429**, 348–352 (2006)
93. Ruan, J.M., Zou, J.P., Zhou, Z.C.: Hydroxyapatite-316L stainless steel fibre composite biomaterials fabricated by hot pressing. Powder Metall. **49**(1), 62–65 (2006)
94. Khalil, K.A., Kim, H.Y., Kim, S.W., Kim, K.W.: Observation of toughness improvement of the hydroxyapatite bioceramics densified using high-frequency induction heat sintering. Int. J. Appl. Ceram. Technol. **4**(1), 30–37 (2007)
95. Bakshi, S.R., Musaramthota, V., Lahiri, D., Singh, V., Seal, S., Agarwal, A.: Spark plasma sintered tantalum carbide: effect of pressure and nano-boron carbide addition on microstructure and mechanical properties. Mater. Sci. Eng. A. **528**, 1287–1295 (2011)
96. Thangamani, N., Chinnakali, K., Gnanam, F.D.: The effect of powder processing on densification, microstructure and mechanical properties of hydroxyapatite. Ceram. Int. **28**, 355–362 (2002)
97. Kobayashi, S., Kawai, W., Wakayama, S.: The effect of pressure during sintering on the strength and the fracture toughness of hydroxyapatite ceramics. J. Mater. Sci. Mater. Med. **17**, 1089–1093 (2006)
98. Veljović, D., Vuković, G., Steins, I., Palcevskis, E., Uskoković, P.S., Petrović, R., Janaćković, D.: Improvement of the mechanical properties of spark plasma sintered HAp bioceramics by decreasing the grain size and by adding multi-walled carbon nanotubes. Sci. Sinter. **45**, 233–243 (2013)
99. Gautier, S., Champion, E., Bernache-Assollant, D.: Toughening characterization in alumina platelets-hydroxyapatite matrix composites. J. Mater. Sci. Mater. Med. **10**, 533–540 (1999)
100. Martin, R.I., Brown, P.W.: Mechanical properties of hydroxyapatite formed at physiological temperature. J. Mater. Sci. Mater. Med. **6**, 138–143 (1995)
101. Will, J., Melcher, R., Treul, C., Travitzky, N., Kneser, U., Polykandriotis, E., Horch, R., Greil, P.: Porous ceramic bone scaffolds for vascularized bone tissue regeneration. J. Mater. Sci. Mater. Med. **19**, 2781–2790 (2008)
102. Rodríguez-Lorenzo, L.M., Vallet-Regí, M., Ferreira, J.M.F.: Fabrication of hydroxyapatite bodies by uniaxial pressing from a precipitated powder. Biomaterials. **22**, 583–588 (2001)
103. Hannora, A.E.: Preparation and characterization of hydroxyapatite/alumina nanocomposites by high-energy vibratory ball milling. J. Ceram. Sci. Technol. **5**(4), 293–298 (2014)
104. Gu, Y.W., Khor, K.A., Cheang, P.: Bone-like apatite layer formation on hydroxyapatite prepared by spark plasma sintering (SPS). Biomaterials. **25**, 4127–4134 (2004)
105. Yasuda, H.Y., Mahara, S., Terashita, N., Umakoshi, Y.: Preparation of porous hydroxyapatite/α-tricalcium phosphate composites by a colloidal process. Mater. Trans. **43**(6), 1332–1335 (2002)
106. Chumnanklang, R., Panyathanmaporn, T., Sitthiseripratip, K., Suwanprateeb, J.: 3D printing of hydroxyapatite: effect of binder concentration in pre-coated particle on part strength. Mater. Sci. Eng. C. **27**, 914–921 (2007)
107. Kothapalli, C., Wei, M., Vasiliev, A., Shaw, M.T.: Influence of temperature and concentration on the sintering behavior and mechanical properties of hydroxyapatite. Acta Mater. **52**, 5655–5663 (2004)
108. Aminzare, M., Eskandari, A., Baroonian, M.H., Berenov, A., Hesabi, Z.R., Taheri, M., Sadrnezhaad, S.K.: Hydroxyapatite nanocomposites: synthesis, sintering and mechanical properties. Ceram. Int. **39**, 2197–2206 (2013)
109. Zhang, J., Maeda, M., Kotobuki, N., Hirose, M., Ohgushi, H., Jiang, D., Iwasa, M.: Aqueous processing of hydroxyapatite. Mater. Chem. Phys. **99**, 398–404 (2006)
110. Juang, H.Y., Hon, M.H.: The effect of calcination temperature on the behaviour of HA powder for injection moulding. Ceram. Int. **23**, 383–387 (1997)
111. Chen, B., Zhang, Z., Zhang, J., Dong, M., Jiang, D.: Aqueous gelcasting of hydroxyapatite. Mater. Sci. Eng. A. **435-436**, 198–203 (2006)

112. Chern Lin, J.H., Lin, H.J., Ding, S.J., Ju, C.P.: Characterization of immersed hydroxyapatite-bioactive glass coatings in Hank's solution. Mater. Chem. Phys. **64**, 229–240 (2000)
113. Hae-Won, K., Young-Hag, K., Seung-Beom, S., Hyoun-Ee, K.: Properties of fluoridated hydroxyapatite-alumina biological composites densified with addition of CaF_2. Mater. Sci. Eng. C. **23**, 515–521 (2003)
114. Rouahi, M., Champion, E., Gallet, O., Jada, A., Anselme, K.: Physico-chemical characteristics and protein adsorption potential of hydroxyapatite particles: influence on in vitro biocompatibility of ceramics after sintering. Colloids Surf. B: Biointerfaces. **47**, 10–19 (2006)
115. Guo, X., Gough, J.E., Xiao, P., Liu, J., Shen, Z.: Fabrication of nanostructured hydroxyapatite and analysis of human osteoblastic cellular response. J. Biomed. Mater. Res. **82A**(4), 1022–1032 (2007)
116. Lin, F.H., Liao, C.J., Chen, K.S., Sun, J.S., Lin, C.P.: Petal-like apatite formed on the surface of tricalcium phosphate ceramic after soaking in distilled water. Biomaterials. **22**, 2981–2992 (2001)
117. Kon, M., Ishikawa, K., Miyamoto, Y., Asaoka, K.: Development of calcium phosphate based functional gradient bioceramics. Biomaterials. **16**, 709–714 (1995)
118. Santos, J.D., Knowles, J.C., Reis, R.L., Monteiro, F.J., Hastings, G.W.: Microstructural characterizations of glass-reinforced hydroxyapatite composites. Biomaterials. **15**(1), 5–10 (1994)
119. Xin, R., Leng, Y., Chen, J., Zhang, Q.: A comparative study of calcium phosphate formation on bioceramics in vitro and in vivo. Biomaterials. **26**, 6477–6486 (2005)
120. Ślósarczyk, A., Piekarczyk, J.: Ceramic materials on the basis of hydroxyapatite and tricalcium phosphate. Ceram. Int. **25**, 561–565 (1999)
121. Evis, Z., Tahmasebifar, A.: Structural and mechanical characteristics of hydroxyapatite and tricalcium phosphates doped with Al^{+3} and F^{-} ions. J. Ceram. Process. Res. **14**, 549–556 (2013)
122. Suchanek, W., Yashima, M., Kakihana, M., Yoshimura, M.: Hydroxyapatite ceramics with selected sintering additives. Biomaterials. **18**, 923–933 (1997)

Publisher's note Springer Nature remains neutral with regard to jurisdictional claims in published maps and institutional affiliations.